The raindrop size distribution - the unknown that holds everything together

Schleiss, Marc; Raupach, Timothy H.; Berne, Alexis

DOI
10.1049/sbra557g_ch6

Publication date
2023

Document Version
Final published version

Published in
Advances in Weather Radar. Volume 2

Citation (APA)
Schleiss, M., Raupach, T. H., & Berne, A. (2023). The raindrop size distribution - the unknown that holds everything together. In V. N. Bringi, K. V. Mishra, & M. Thurai (Eds.), *Advances in Weather Radar. Volume 2: Precipitation Science, Scattering and Processing Algorithms* (Vol. 2, pp. 247-292). Institution of Engineering and Technology. https://doi.org/10.1049/sbra557g_ch6

Chapter 6

The raindrop size distribution – the unknown that holds everything together

Marc Schleiss[1], Timothy H. Raupach[2] and Alexis Berne[3]

6.1 Introduction

The raindrop size distribution (DSD) is a statistical description of the number and size distribution of raindrops within a specified volume of air. DSDs play a central role in radar remote sensing and are essential for understanding the scattering and absorption of electromagnetic radiation as it travels through the air and interacts with falling rain. They form the mathematical backbone for linking radar observations to physical quantities such as rainfall intensities, liquid water content, and kinetic energy. Yet, in most remote sensing applications, the DSD in the target volume is likely to be unknown. Therefore, parameterized DSD models have been created to act as substitutes for direct measurements when observations are unavailable, incomplete, or impractical. Over time, a large number of models have been proposed, each with their own intricacies and constraints. Understanding these mathematical constructs and the assumptions behind them is essential for interpreting radar measurements and improving quantitative rainfall estimation.

The most widely used DSD models to date are the exponential, the gamma, the lognormal and the generalized gamma distribution (which includes the Weibull distribution as a special case). For each model, different special cases, normalized formulations or constrained versions exist. The literature on the topic is vast and rather overwhelming. Therefore, we thought that it is valuable to summarize the essence of the work in a few pages, by compiling a list of the most common models, their properties, and their usage across disciplines, with a special focus on weather-radar-related applications and numerical weather prediction. Due to the enormity of the task, the list we provide is far from complete. For example, non-parametric models

[1]Department of Geoscience and Remote Sensing, Delft University of Technology (TU Delft), The Netherlands
[2]Climate Change Research Centre and ARC Centre of Excellence for Climate Extremes, University of New South Wales, Australia
[3]Environmental Remote Sensing Laboratory (LTE), École Polytechnique Fédérale de Lausanne, Switzerland

and other, more empirical ways of describing DSDs will not be considered. Nevertheless, what follows probably represents the largest and most detailed compilation of available DSD models in a single publication to date. By effectively summarizing the information scattered across hundreds of publications and decades of research using consistent notations and units, we hope to make it easier for others to understand the logic behind different DSD representations and help them select the most appropriate representation for a given task.

The rest of this chapter is structured as follows. Section 6.2 introduces the DSD, its statistical moments, and related bulk variables. Section 6.3 introduces the basic principles behind parametric DSD modeling and draws up an inventory of the most common models and their key mathematical properties. Section 6.4 addresses the issue of DSD normalization and presents the mathematical frameworks for single, double, and multi-moment normalization of DSDs. Section 6.5 briefly summarizes the role played by DSDs in weather radar together with some techniques for retrieving DSDs from polarimetric radar observations. Section 6.6 provides a brief overview of how DSDs are represented in numerical weather prediction models, with some notes and caveats. Conclusions and recommendations for future developments are given in Section 6.7.

6.2 The DSD and its statistical moments

The main motivation for studying raindrop size distributions is that most rainfall-related variables can be written as weighted combinations of the statistical moments of the DSD. Essentially, if we know the DSD, then we can calculate any rainfall variable of interest using its moments. In this section, we introduce, mathematically, the DSD, its moments, and variables defined using DSD moments.

The raindrop size distribution

The raindrop size distribution $N(D)$ ($\mathrm{mm}^{-1}\ \mathrm{m}^{-3}$) is the concentration of raindrops of diameter D (mm) per unit volume of air. We write

$$N(D) = N_T f(D), \tag{6.1}$$

where

$$N_T = \int_0^\infty N(D) dD \tag{6.2}$$

is the total number concentration of raindrops (m^{-3}) and $f(D)$ (mm^{-1}) is a probability density function for the drop diameters such that $\int_0^\infty f(D) = 1$ and $\mathbb{P}[D \leq x] = \int_0^x f(D) dD$ where $\mathbb{P}$ is the probability operator.

By convention, what we refer to as the raindrop diameter D is actually the diameter of a sphere with the same volume as the raindrop – the "equivolume diameter." This convention is important since larger raindrops are oblate, owing to the aerodynamic forces acting on them [1–3]. It is also important to note that the raindrop size distribution as defined above only describes the average conditions in a specified volume of air. In reality, the local concentrations of raindrops, their positions, and sizes all fluctuate over space and time [4–7]. The DSD should, therefore, be seen as a probabilistic summary of the average (i.e., the expected) raindrop size distribution over a large number of unit volumes. For weather-radar-related applications, this assumption is reasonable because radar sampling volumes are generally much larger than one cubic meter.

Statistical moments of the DSD

The nth-order moment M_n ($\text{mm}^n\ \text{m}^{-3}$) of the DSD is defined as

$$M_n = \int_0^\infty D^n N(D) dD. \tag{6.3}$$

Combinations of weighted moments of the DSD give rainfall properties of interest. Different moments are used in different contexts. For example, the zeroth-order moment is the total number concentration N_T (m^{-3}), while the first-order moment is related to the mean drop diameter. For visibility studies (e.g., optical extinction), the second-order moment is the most relevant [8]. The liquid water content (LWC) is linked to the third-order moment, and the rainfall rate is approximately proportional to the 3.67th-order moment [9] via (6.11). The kinetic energy is roughly proportional to the fifth-order moment [10], and microwave backscatter (e.g., radar reflectivity) is equal to the sixth-order moment in the Rayleigh scattering regime [11]. Most radar remote-sensing applications rely heavily on higher-order moments of the DSD, while microphysical processes in rain, such as collisional drop breakup, coalescence, and evaporation, also depend on lower-order moments [12–15]. Higher-order moments are more sensitive to the concentration of large drops than lower-order moments. This is why a few large drops will affect rain rate and radar reflectivity substantially, while having very little impact on the mean drop diameter and drop number concentration.

It is important to note that for simplicity, in this chapter, the raindrop diameter integration limits are assumed to be 0 to ∞, so any truncation of the size distribution between a lower drop diameter limit $D_{\min}$ and upper limit $D_{\max}$ is ignored. In reality, there are clear physical limits on how small or large raindrops can become [16,17]. For example, thermodynamic calculations show that raindrops with diameters below 0.1 mm usually cannot fall much more than 100–200 m before evaporating [18,19]. On the other hand, the larger a raindrop becomes, the more likely it is to collide with other drops and break up into smaller pieces [17]. Very large raindrops with diameters above 10 mm are so hydrodynamically unstable that they spontaneously break up due to aerodynamic forces, even in laminar air flows [17]. In turbulent

conditions, the forces acting on raindrops tend to be stronger, which explains why the vast majority of raindrops have diameters smaller than 5 mm [20]. One study [20] showed that only 0.4% of more than 775,000 one-min raindrop spectra at 17 locations contained drops with diameters larger than 5 mm, with tropical locations accounting for most of those. Another fact that should be pointed out is that most commercially available DSD sensors have some form of limitation on the minimum and maximum drop sizes that can be measured [21,22]. For example, an experiment [22] in which a commonly used optical disdrometer was collocated with a higher-resolution sensor showed that the optical disdrometer was not properly capturing the "drizzle mode," i.e., the drops with $D < 0.5$ mm. This discovery led to the introduction of more general functional forms for modeling the DSD that properly model the drizzle mode [23], as well as new techniques to "reconstruct" the full DSD from measurements made by DSD sensors in which truncation precludes accurate representations of the smallest drops [24]. Truncation of the DSDs at the lower or upper ends of the spectrum owing to instrumental limitations, and discretization effects owing to limited resolution and size binning, are serious issues that affect the calculation of DSD moments to varying degrees depending on the moment order and the nature of the truncation or binning [16,25,26]. However, since these limitations are highly specific to the given sensor, we decided not to consider them here.

In the following sections, we describe the different types of variables that can be calculated from the DSD: state variables, which describe the properties of raindrops in a fixed volume of air; flux variables, which describe raindrops arriving at a surface (Figure 6.1 illustrates the difference between state and flux variables); and variables that describe a "characteristic" raindrop size.

6.2.1 State variables

State variables describe the properties of raindrops in a fixed volume of air (Figure 6.1). In this section, different state variables are introduced by ascending order of DSD moment.

Total number concentration

The total number concentration of raindrops N_T (m^{-3}), as previously defined in (6.2) is

$$N_T = \int_0^\infty N(D)dD = M_0. \tag{6.4}$$

The total number concentration plays a crucial role in the study of microphysical processes such as collisional drop growth, breakup, and evaporation [14,15]. Typical values of N_T are in the order of 100–1,000 m^{-3} but can exceed 10^4 m^{-3} in heavy rain [27]. In general, N_T tends to increase with rainfall intensity. However, peak raindrop concentration values are not necessarily associated with the highest rainfall rates [28,29] and large concentrations of small drops ($D < 0.7$ mm) can also be found

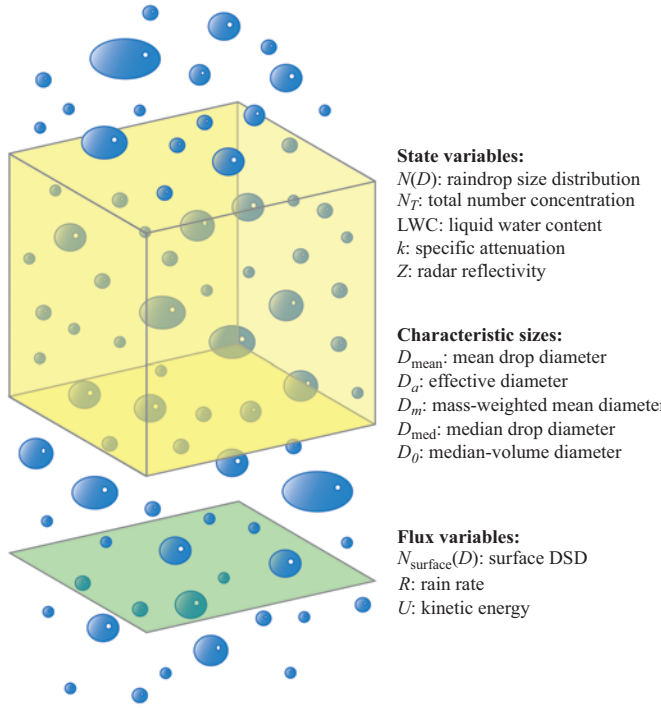

Figure 6.1 Schematic illustrating the conceptual differences between the types of DSD variables. State variables describe the raindrops within a volume of air, like those inside the yellow box in this diagram. Characteristic sizes describe the "characteristic" size of the raindrops in the DSD volume. Flux variables describe raindrops arriving at a surface, such as those crossing the green surface shown here.

in drizzle [23]. Accurately measuring N_T is challenging and substantial bias can be introduced in N_T estimates owing to instruments' small sampling surfaces and small-drop truncations of the size spectra [30–32]. Consequently, many experts nowadays prefer to work with a less sensitive concentration-related variable N_w, which is based on the notion of normalized drop size spectra (see Sections 6.4, (6.32) and (6.34) for more details).

Liquid water content

The liquid water content LWC (g m^{-3}) is

$$\text{LWC} = \frac{\pi \rho_W}{6{,}000} \int_0^\infty D^3 N(D) dD = \frac{\pi \rho_W}{6{,}000} M_3, \tag{6.5}$$

where $\rho_W \approx 1$ g cm^{-3} is the density of liquid water.

Liquid water content is an important parameter that influences the dynamical structure and radiative characteristics of clouds [33]. In clouds, it is dependent on cloud type, cloud-based temperature, and cloud vertical extent, and often correlates well with flux variables such as the rainfall rate [34]. In rain, typical values of LWC range between 0.1 g m^{-3} in stratiform rain and 0.5 g m^{-3} in cumulus clouds [35] and 1–3 g m^{-3} in severe thunderstorms [36]. However, over short-time scales, values exceeding 10 g m^{-3} in extreme precipitation and tropical cyclones have been measured [37,38].

Specific attenuation

The specific attenuation k (dB km^{-1}) of a microwave signal traversing a uniform rainfall field with a given DSD is

$$k = \frac{1}{\ln(10)} \int_0^\infty \sigma_E(D) N(D) dD, \tag{6.6}$$

where $\sigma_E(D)$ (cm^2) is the extinction cross-section of a raindrop of diameter D.

Specific attenuation is of paramount importance for the calculation of path-averaged attenuation of electromagnetic radiation transmitted across terrestrial links [39] as well as for performing attenuation correction in radar and satellite-based remote-sensing applications [40–42]. For terrestrial links, specific attenuation is often assumed to be a power law of the rainfall intensity [43]. In general, $\sigma_E(D)$ depends on the wavelength of the electromagnetic signal and the temperature of the drop. The general theory for how to calculate $\sigma_E(D)$ using electromagnetic scattering theory is beyond the scope of this chapter. However, three particular cases can be distinguished: when the wavelength of the signal is comparable to the raindrop diameter, extinction cross-sections can be calculated using Mie scattering [44]. When the raindrops are much smaller than the wavelength, Rayleigh scattering can be assumed [45]. And, in the limit where the raindrop diameters greatly exceed the wavelength (e.g., as is the case for optical signals), $\sigma_E(D)$ is equal to twice the geometric cross-section and k becomes proportional to the second-order moment of the DSD [46].

Radar reflectivity factor

The effective radar reflectivity factor Z (mm^6 m^{-3}) in the Rayleigh limit (i.e., large wavelength, without attenuation) is given by

$$Z = \int_0^\infty D^6 N(D) dD = M_6. \tag{6.7}$$

The radar reflectivity factor Z is the sixth-order moment of the DSD [47]. Because it can span a huge range of magnitudes, from 0.001 mm^6 m^{-3} in fog up to several

million $\text{mm}^6\ \text{m}^{-3}$ in extremely heavy rain [48], it is common to express it in decibels (dB) of Z, also known as dBZ, calculated as $10\log_{10}(Z)$. Note that the definition above is a purely theoretical quantity that assumes perfect calibration, Rayleigh scattering, no attenuation, no shielding and no anomalous propagation, and is, therefore, independent of any actual radar property.

6.2.2 Flux variables

Flux variables describe the properties of rainfall over a unit surface area. Fluxes are different from state variables such as N_T, LWC, and Z in the sense that they do not solely depend on the number concentration and size distribution of raindrops but also on the rate at which raindrops of a given size arrive at the surface. Consequently, the fall velocity $v(D)$ of raindrops with respect to their diameter must also be considered [49,50]. This is a vast and important topic that goes well beyond the scope of this chapter. For the sake of simplicity, we will assume that the average fall velocity $v(D)$ (in $\text{m}\ \text{s}^{-1}$) of a raindrop with diameter D (in mm) can be reasonably well approximately by a power law, such that

$$v(D) = a_v D^{b_v}, \tag{6.8}$$

where $a_v > 0$ ($\text{m}\ \text{s}^{-1}\ \text{mm}^{-b_v}$) and $b_v > 0$ (unitless) are two positive coefficients [51]. In fact, the power-law model is the only functional form that leads to a power-law relationship between rainfall rate and reflectivity, as is commonly assumed [27]. Commonly accepted values for standard conditions of temperature and pressure are $a_v = 3.778\ \text{m}\ \text{s}^{-1}\ \text{mm}^{-0.67}$ and $b_v = 0.67$ [39]. Additional corrections for the changing air density and temperature with height can be made [49,52]. Note that the power-law model above only describes the theoretical fall velocity of a drop in still air, which, according to [53], should be reached after a relatively short fall distance in the order of 10 m. In reality, the fall speeds of individual drops frequently change due to microphysical processes such as drop coalescence, breakup and evaporation. For example, several studies show that intermediate-sized raindrops can fall up to an order of magnitude faster than expected [54,55]. The vertical wind speeds and turbulence of the air also play a crucial role [56].

DSD at the surface

The DSD at the surface, over a unit time interval and measurement area is

$$N_{\text{surface}}(D) = v(D)N(D) \approx a_v D^{b_v} N(D). \tag{6.9}$$

The vast majority of weather-radar-related studies use the traditional definition of the DSD in a unit volume (Equation (6.1)). However, because raindrops of different sizes fall at different velocities, the DSD in a unit volume of air will be different from the DSD seen by a fixed observer on the ground. As long as the fall velocities of the raindrops are known, the volume and surface representations of $N(D)$ are perfectly interchangeable. However, in practice, going from one representation to

another inevitably introduces some additional uncertainty owing to the fact that the actual fall speeds of raindrops can substantially deviate from theoretical relationships. For example, fall speeds depend on local wind patterns including updrafts and downdrafts, as well as pressure and temperature [52,54,56]. For some applications, it may be beneficial to directly model the DSD at the surface using marked point processes and inter-drop arrival time distributions [57,58]. These methods only consider the sizes and arrival process of raindrops at the surface, from which all relevant fluxes can be computed independently of any assumptions about drop velocities. It is worth noting that the most common type of sensor for measuring drop size distributions, the optical disdrometer, actually measures the surface DSD. The measurements are then transformed back to a unit volume using the measured fall velocities of each drop or a theoretical fall velocity model as in (6.9). Sensors capable of directly estimating the DSD in a three-dimensional volume exist and avoid this issue, but are technologically challenging and to date have mostly been used for studying snow and ice particles [59–63].

Rainfall rate

The rainfall rate R (mm h^{-1}) is the average flux of water through a unit area

$$R = 6\pi 10^{-4} \int_0^\infty D^3 N(D) v(D) dD. \tag{6.10}$$

If raindrop fall velocities are assumed to follow a power law (6.8) with $a_v = 3.778$ and $b_v = 0.67$, then

$$\begin{aligned} R &\approx 6\pi 10^{-4} a_v M_{3+b_v} \\ &\approx 0.0071 M_{3.67}. \end{aligned} \tag{6.11}$$

Equation (6.11) shows that the rainfall rate R is approximately proportional to the DSD's moment of order 3.67, which makes it closely related to the liquid water content. Rainfall rate is the main quantity of interest in hydrological sciences and quantitative precipitation estimation using weather radar [64–67]. Typical rainfall rates at the hourly time scale are <0.1 mm h^{-1} in drizzle [68], up to 2.5 mm h^{-1} in light rain, up to 10 mm h^{-1} in moderate rain, up to 50 mm h^{-1} in heavy rain, and ≥ 50 mm h^{-1} in extremely intense rainfall [69]. However, there is no commonly agreed-upon standard for classifying rain rates, and each meteorological agency uses slightly different definitions depending on the local climatology. Distributions of R are heavily skewed and approximately lognormal or gamma, but strongly depend on the local climatology, aggregation time scale and type of event [70–72]. Because the fall velocity of raindrops varies with altitude [50], the value of R for a given DSD also varies with altitude. This dependence on altitude makes the definition of rain rate in (6.11) somewhat ambiguous. To avoid this issue and compare rain rates in weather radar data on a fair basis, rates are often calculated for ground level by assuming a fixed fall-velocity model that is independent of height [73].

Kinetic energy

The kinetic energy flux density U (J m^{-2} s^{-1}) is

$$U = \frac{\pi}{12}\rho_W 10^{-6}\int_0^\infty D^3 v(D)^3 N(D) dD. \tag{6.12}$$

Assuming drop fall velocities follow a power law (6.8) with $a_v = 3.778$ and $b_v = 0.67$, and assuming $\rho_W = 1$ g cm^{-3}, we have

$$U \approx \frac{\pi}{12}\rho_W 10^{-6} a_v^3 M_{3+3b_v} \approx 14.12 \cdot 10^{-6} M_{5.01}. \tag{6.13}$$

Kinetic energy plays a crucial role in understanding soil erosion, soil loss and sediment transport [74–78], as well as in monitoring and predicting the erosion of wind-turbine blades used in wind energy production [79,80]. Kinetic energy of rainfall may also play an important role in the growth and development of vegetation. For example, the authors of [81] showed that the immune system of *Arabidopsis thaliana* activates itself against pathogens in response to impacting raindrops. The *Arabidopsis* response is mechanic, meaning that the raindrops need to impact with a certain energy to trigger a response [81].

6.2.3 Characteristic sizes

When comparing and summarizing DSDs, it is often useful to consider the "characteristic" raindrop size. Depending on the application, different characteristic sizes may be of interest. Quantities such as the mean drop diameter and median drop diameter are natural choices. However, they may not be the best characteristic size descriptors for radar-related applications [48,82]. For this reason, other sizes related to higher moments or ratios of moments have been defined.

Weighted mean drop diameters

Weighted mean drop diameters are ratios of successive moments of the DSD. For example, the mean drop diameter D_{mean} (mm) is the ratio between the first- and zeroth-order moments of the DSD, such that

$$D_{\text{mean}} = \frac{1}{N_T}\int_0^\infty DN(D) dD = \frac{M_1}{M_0}. \tag{6.14}$$

The area-weighted mean drop diameter D_a (mm), also known as the "effective diameter," is

$$D_a = \frac{\int_0^\infty D^3 N(D) dD}{\int_0^\infty D^2 N(D) dD} = \frac{M_3}{M_2}. \tag{6.15}$$

A commonly used characteristic diameter is the mass- (or volume-) weighted mean drop diameter D_m (mm), which is written

$$D_m = \frac{\int_0^\infty D^4 N(D) dD}{\int_0^\infty D^3 N(D) dD} = \frac{M_4}{M_3}. \tag{6.16}$$

Typical values for D_m range between 0.5 mm and 4.0 mm, with average values around 1 mm [35,83,84].

Median drop diameters

The median drop diameter D_{med} (mm) is the diameter that divides the population of drops in half by size, such that half of the drops are smaller and half are larger than D_{med}. We write

$$2\int_0^{D_{\text{med}}} N(D) dD = \int_0^\infty N(D) dD. \tag{6.17}$$

Median drop sizes can also be derived for higher-order moments of the DSD. For example, the median-volume diameter D_0 (mm) divides the DSD such that half of the liquid water content is due to drops with diameters greater than D_0 [8], such that

$$2\int_0^{D_0} D^3 N(D) dD = \int_0^\infty D^3 N(D) dD. \tag{6.18}$$

Similar definitions of D_{med} and D_0 based on the DSD seen by a fixed observer at the surface are also possible [27] but are less commonly used.

Weighted mean drop diameters and median drop diameters provide similar information and are closely linked [9]. The advantage of weighted moments such as D_m is that they are slightly easier to calculate in practice, since disdrometers often bin the drop counts into different diameter classes. This discretization means that median drop diameters can only be determined using interpolation, which introduces additional uncertainty compared to an integration over the whole size spectrum.

6.3 Parametric DSD models

DSD models require abstraction and simplification. In practice, this means identifying, selecting, and summarizing relevant aspects of the rainfall process. The properties

that are the most relevant may vary from one application to another, which explains why most DSD models are heavily task-driven: they were developed with a certain objective in mind. Examples of tasks that use DSD models include quantitative estimation of precipitation from weather radar, microphysical retrievals, radar attenuation correction, stochastic simulation of rainfall time series, and numerical weather prediction. The diversity of these tasks means that the "best" DSD models are not necessarily the ones that provide the best fit to the data, but the ones that work in practice and are useful for understanding the problem at hand. Quantitative radar-rainfall retrieval algorithms, for example, often adopt rather simplistic parametric DSD models with one or two degrees of freedom. There are two main reasons for this. First, radars can only measure a small number of DSD moments (see Section 6.5.3), which limits the number of parameters that can be estimated. Second, radar measurements are subject to stochastic noise and various types of biases [66,85]. Fitting complex models to noisy data is bad practice, which explains why simple DSD models are often the best choice in operational settings. Simple low-dimensional models may not be as good as more complex models at reproducing the large diversity of possible DSD shapes that can exist, but they are substantially more robust to noise and less prone to overfitting.

It is experimentally and theoretically well established that the different microphysical processes that control the evolution of raindrop size distributions (e.g., collisional growth, breakup and evaporation) tend to produce roughly unimodal, positively skewed distributions [86–89]. However, more complex, multi-modal DSDs associated with transitional regimes and mixed-phase precipitation have also been observed [87,90,91].

When choosing a model, one should take into account that substantial differences may exist between the measured and actual shapes of DSDs, owing to instrumental effects/limitations, random sampling effects and environmental conditions such as wind and turbulence. For example, optical disdrometers are notoriously bad at measuring small drop diameters below 0.3 mm which is a serious problem during light rain and drizzle and may cause lower order moments to be affected by substantial biases [22,24]. As a result, it is often very difficult to objectively decide which model amongst many candidate models provides the best fit to the data.

6.3.1 Inventory of common DSD models

The most common parametric models for representing DSDs are the Exponential [92], the Gamma [9,25], the Lognormal [93], and generalized Gamma [94,95] models. Less common choices include the Weibull [96], the Beta [97], and the Johnson SB [98] models. Flashcards describing the most-popular DSD models are shown below, together with their key mathematical properties. Each model is summarized on a single page, which restricts our treatment to only the most essential properties. Nevertheless, we believe that providing such an overview, using consistent notations and units is of great value to the community. Figures 6.2 and 6.3 show example shapes for the models presented in this section.

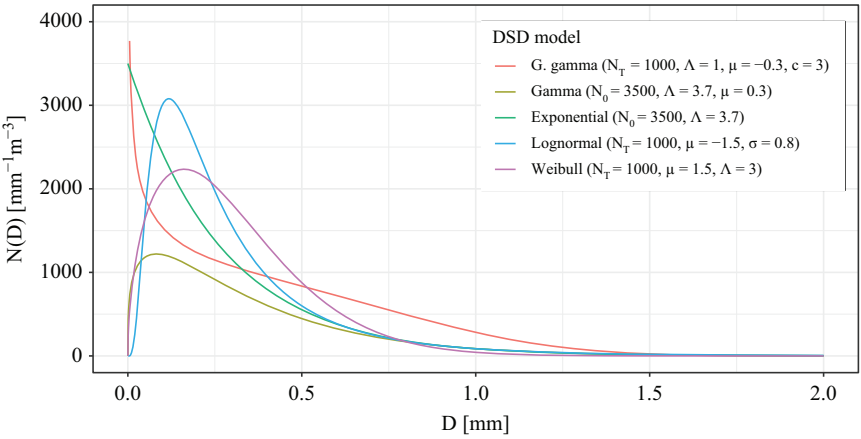

Figure 6.2 Example of DSD models (on a linear scale) with parameters chosen to show different possible shapes for each model. "G. gamma" stands for the generalized gamma model, which can have very different shapes from the other models depending on its parameters. See the flashcards for each model for descriptions and units of parameters.

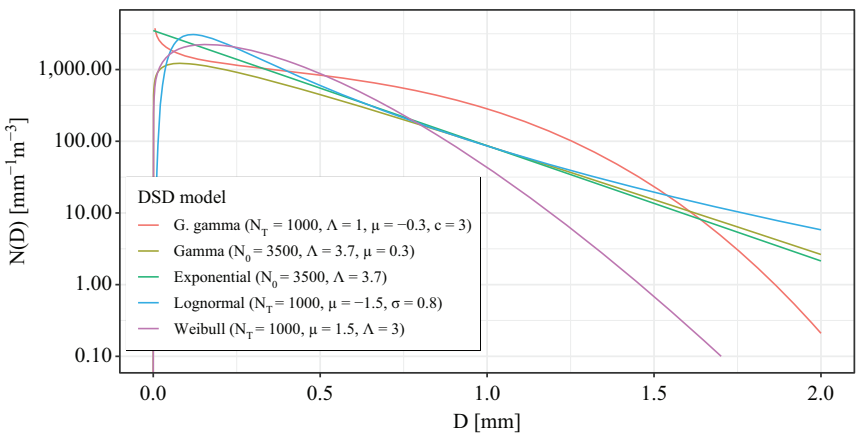

Figure 6.3 As in Figure 6.2, but with a logarithmic y-axis to show details of differences at the larger drop end of the spectrum

Exponential

$$N(D) = N_0 \exp(-\Lambda D)$$

Parameters: intercept N_0 ($\text{mm}^{-1}\ \text{m}^{-3}$), slope Λ (mm^{-1}).

Explanations: the simple exponential DSD model proposed by Marshall and Palmer (MP) in 1948 [92] is the most-cited in radar meteorology and still used today. It provides a good approximation of average DSDs over large measurement volumes [99] using a small number of parameters with clear, physical interpretations.

Moments:

$$M_n = N_0 \frac{\Gamma(n+1)}{\Lambda^{n+1}} \quad \frac{M_n}{M_m} = \frac{\Gamma(n+1)}{\Gamma(m+1)} \Lambda^{m-n}$$

State variables:

$$N_T = \frac{N_0}{\Lambda} \quad \text{LWC} = \frac{N_0 \pi \rho_W}{1000 \Lambda^4} \quad Z = 720 N_0 \Lambda^{-7}$$

Characteristic sizes:

$$D_{\text{mean}} = \frac{1}{\Lambda} \quad D_a = \frac{3}{\Lambda} \quad D_m = \frac{4}{\Lambda} \quad D_{\text{med}} = \frac{\ln(2)}{\Lambda} \quad D_0 \approx \frac{3.67}{\Lambda}$$

Fluxes:

$$R \approx 6\pi 10^{-4} a_v N_0 \frac{\Gamma(4+b_v)}{\Lambda^{4+b_v}} \approx 0.105 \frac{N_0}{\Lambda^{4.67}}$$

$$U \approx \frac{\pi}{12} \rho_W 10^{-6} a_v^3 N_0 \frac{\Gamma(4+3b_v)}{\Lambda^{4+3b_v}} \approx 14.12 \cdot 10^{-6} N_0 \frac{\Gamma(6.01)}{\Lambda^{6.01}}$$

Notes: if $N(D)$ is exponential and $v(D) = a_v D^{b_v}$, then $N_{\text{surface}}(D)$ is gamma with concentration $a_V N_0$, shape b_V and slope Λ. The original model [92] is a particular case of an exponential DSD with a fixed concentration parameter N_0 = 8,000 ($\text{mm}^{-1}\text{m}^{-3}$) and only one free parameter Λ. The slope of such a DSD depends solely on R. Using a graph paper, MP found that $\Lambda = 4.1 R^{-0.21}$ [92], which is only slightly different from the theoretical relation $\Lambda = 4.23 R^{-0.21}$ obtained by assuming $v(D) = 3.778 D^{0.67}$ [51].

Gamma

$$N(D) = N_0 D^{\mu} \exp(-\Lambda D)$$

Parameters: slope Λ (mm^{-1}), shape μ (-), concentration N_0 (m^{-3} $\mathrm{mm}^{-1-\mu}$).

Explanations: the gamma distribution [9] is the most popular DSD model in use today. The shape parameter μ provides additional flexibility over the exponential model, which leads to better fits at high temporal resolutions and in convective rain [100,101].

Moments:

$$M_n = N_0 \frac{\Gamma(\mu + n + 1)}{\Lambda^{\mu+n+1}} \quad \frac{M_n}{M_m} = \Lambda^{m-n} \frac{\Gamma(\mu + n + 1)}{\Gamma(\mu + m + 1)}$$

State variables:

$$N_T = N_0 \frac{\Gamma(\mu + 1)}{\Lambda^{\mu+1}} \quad \mathrm{LWC} = N_0 \frac{\pi \rho_W}{6000} \frac{\Gamma(\mu + 4)}{\Lambda^{\mu+4}} \quad Z = N_0 \frac{\Gamma(\mu + 7)}{\Lambda^{\mu+7}}$$

Characteristic sizes:

$$D_{\mathrm{mean}} = \frac{\mu + 1}{\Lambda} \quad D_a = \frac{\mu + 3}{\Lambda} \quad D_m = \frac{\mu + 4}{\Lambda}$$

$$D_{\mathrm{med}} \approx \frac{\mu + 1}{\Lambda} \left(1 - \frac{1}{9(\mu + 1)}\right)^3 \quad D_0 \approx \frac{\mu + 3.67}{\Lambda}$$

Fluxes:

$$R \approx 6\pi 10^{-4} a_v N_0 \frac{\Gamma(\mu + 4 + b_v)}{\Lambda^{\mu+4+b_v}} \approx 0.0071 N_0 \frac{\Gamma(\mu + 4.67)}{\Lambda^{\mu+4.67}}$$

$$U \approx \frac{\pi}{12} \rho_W 10^{-6} a_V^3 N_0 \frac{\Gamma(\mu + 4 + 3b_V)}{\Lambda^{\mu+4+3b_V}} \approx 14.12 \cdot 10^{-6} N_0 \frac{\Gamma(\mu + 6.01)}{\Lambda^{\mu+6.01}}$$

Notes: when $\mu = 0$, the gamma model reduces to an exponential. For positive μ, the DSD is concave down on a plot of $\ln N(D)$ vs D and rapidly falls to zero for larger values of D. For negative μ, the DSD is concave upward with a larger spread [9]. If $N(D)$ is gamma and $v(D) = a_V D^{b_V}$, then $N_{\mathrm{surface}}(D)$ is gamma with intercept $a_V N_0$, shape $\mu + b_V$ and slope Λ. Based on empirical evidence, some studies have suggested a deterministic relationship between μ and Λ. For example, the authors of [102,103] recommend $\Lambda = 0.0365\mu^2 + 0.735\mu + 1.935$.

Generalized gamma

$$N(D) = N_T \Gamma\left(\frac{\mu+1}{c}\right)^{-1} c\Lambda^{\mu+1} D^{\mu} \exp\left(-(\Lambda D)^c\right)$$

Parameters: generalized shape $\mu > -1$, slope $\Lambda > 0$, coefficient $c > 0$.

Explanations: the generalized gamma [95,104] is popular and fits well to a wide variety of particle distributions including those of cloud droplets and ice particles. c can be tuned to improve the fit in a plateau region and tails [23,24].

Moments:

$$M_n = N_T \left(\frac{1}{\Lambda}\right)^n \frac{\Gamma\left(\frac{\mu+1+n}{c}\right)}{\Gamma\left(\frac{\mu+1}{c}\right)} \quad \frac{M_n}{M_m} = \Lambda^{m-n} \frac{\Gamma\left(\frac{\mu+1+n}{c}\right)}{\Gamma\left(\frac{\mu+1+m}{c}\right)}$$

State variables:

$$LWC = N_T \frac{\pi\rho_W}{6000\Lambda^3} \frac{\Gamma\left(\frac{\mu+4}{c}\right)}{\Gamma\left(\frac{\mu+1}{c}\right)} \quad Z = \frac{N_T}{\Lambda^6} \frac{\Gamma\left(\frac{\mu+7}{c}\right)}{\Gamma\left(\frac{\mu+1}{c}\right)}$$

Characteristic sizes:

$$D_{\text{mean}} = \frac{1}{\Lambda} \frac{\Gamma\left(\frac{\mu+2}{c}\right)}{\Gamma\left(\frac{\mu+1}{c}\right)} \quad D_a = \frac{1}{\Lambda} \frac{\Gamma\left(\frac{\mu+4}{c}\right)}{\Gamma\left(\frac{\mu+3}{c}\right)} \quad D_m = \frac{1}{\Lambda} \frac{\Gamma\left(\frac{\mu+5}{c}\right)}{\Gamma\left(\frac{\mu+4}{c}\right)}$$

Fluxes:

$$R \approx 6\pi 10^{-4} a_V N_T \left(\frac{1}{\Lambda}\right)^{3+b_V} \frac{\Gamma\left(\frac{\mu+b_V+4}{c}\right)}{\Gamma\left(\frac{\mu+1}{c}\right)} \approx 0.0071 N_T \left(\frac{1}{\Lambda}\right)^{3.67} \frac{\Gamma\left(\frac{\mu+4.67}{c}\right)}{\Gamma\left(\frac{\mu+1}{c}\right)}$$

$$U \approx \frac{\pi\rho_W a_V^3 N_T}{12 \cdot 10^6} \left(\frac{1}{\Lambda}\right)^{3+3b_V} \frac{\Gamma\left(\frac{\mu+3b_V+4}{c}\right)}{\Gamma\left(\frac{\mu+1}{c}\right)} \approx \frac{14.12}{10^6} \left(\frac{1}{\Lambda}\right)^{5.01} \frac{\Gamma\left(\frac{\mu+6.01}{c}\right)}{\Gamma\left(\frac{\mu+1}{c}\right)}$$

Notes: the distribution reduces to gamma when $c = 1$, exponential when $c = 1$ and $\mu = 0$, and Weibull when $c = \mu + 1$. [23] showed that $c \approx 2.5$ is the most common value. If $N(D)$ is a generalized gamma and $v(D) = a_V D^{b_V}$, then $N_{\text{surface}}(D)$ is a generalized gamma with shape $\mu + b_V$, slope Λ, coefficient c, and intercept $(N_T a_v)/\Lambda^{b_V} \Gamma\left((\mu + 1 + b_v)/c\right) \left[\Gamma\left((\mu + 1)/c\right)\right]^{-1}$.

Lognormal

$$N(D) = \frac{N_T}{\sqrt{2\pi}\sigma D} \exp\left[-\frac{1}{2}\left(\frac{\ln(D) - \mu}{\sigma}\right)^2\right]$$

Parameters: $\mu \in \mathbb{R}$ and $\sigma > 0$, the mean and standard deviation of $\ln(D)$.

Explanations: the lognormal assumes that $\ln(D)$ has a Gaussian distribution. The lognormal distribution has the advantage of being stable with respect to power transformations, which means that the surface DSD is also lognormal. This property, together with the close link to the Gaussian distribution, makes it particularly appealing for stochastic simulation.

Moments:

$$M_n = N_T \exp\left(n\mu + \frac{1}{2}n^2\sigma^2\right) \quad \frac{M_n}{M_m} = \exp\left((n-m)\mu + \frac{1}{2}(n^2 - m^2)\sigma^2\right)$$

State variables:

$$\mathrm{LWC} = \frac{\pi\rho_W}{6000} N_T \exp\left(3\mu + \frac{9}{2}\sigma^2\right) \quad Z = N_T \exp\left(6\mu + 18\sigma^2\right)$$

Characteristic sizes:

$$D_{\mathrm{mean}} = \exp\left(\mu + \frac{1}{2}\sigma^2\right) \quad D_a = \exp\left(\mu + \frac{5}{2}\sigma^2\right) \quad D_m = \exp\left(\mu + \frac{7}{2}\sigma^2\right)$$

$$D_{\mathrm{med}} = \exp(\mu) \quad D_0 = \exp\left(\mu + 3\sigma^2\right)$$

Fluxes:

$$\begin{aligned} R &\approx 6\pi 10^{-4} a_v N_T \exp\left((3 + b_v)\mu + \frac{(3 + b_v)^2\sigma^2}{2}\right) \\ &\approx 0.0071 N_T \exp\left(3.67\mu + 6.73\sigma^2\right) \\ U &\approx \frac{\pi}{12}\rho_W 10^{-6} a_v^3 N_T \exp\left((3 + 3b_v)\mu + \frac{1}{2}(3 + 3b_v)^2\sigma^2\right) \\ &\approx 14.12 \cdot 10^{-6} N_T \exp\left(5.01\mu + 12.55\sigma^2\right) \end{aligned}$$

Notes: for a lognormal, $N_{\mathrm{surface}}(D)$ is also lognormal with parameters $\mu_{\mathrm{surface}} = b_V(\mu + \ln(a_V))$ and $\sigma_{\mathrm{surface}} = b_V\sigma$.

Weibull

$$N(D) = N_T \mu \Lambda^{\mu} D^{\mu-1} \exp\left[-(\Lambda D)^{\mu}\right]$$

Parameters: shape $\mu \geq 0$, rate $\Lambda > 0$.

Explanations: while the Weibull can provide good fits to individual DSD spectra [105,106], studies have shown that overall, its goodness of fit tends to be slightly inferior to the gamma and lognormal models [107]. As a result, this model is less common in the literature about DSDs.

Moments:

$$M_n = N_T \frac{\Gamma\left(1+\frac{n}{\mu}\right)}{\Lambda^n} \quad \frac{M_n}{M_m} = \Lambda^{m-n} \frac{\Gamma\left(1+\frac{n}{\mu}\right)}{\Gamma\left(1+\frac{m}{\mu}\right)}$$

State variables:

$$\mathrm{LWC} = \frac{\pi \rho_W}{6000} N_T \frac{\Gamma\left(1+\frac{3}{\mu}\right)}{\Lambda^3} \quad Z = N_T \frac{\Gamma\left(1+\frac{6}{\mu}\right)}{\Lambda^6}$$

Characteristic sizes:

$$D_{\mathrm{mean}} = \frac{\Gamma\left(1+\frac{1}{\mu}\right)}{\Lambda} \quad D_a = \frac{\Gamma\left(1+\frac{3}{\mu}\right)}{\Lambda\Gamma\left(1+\frac{2}{\mu}\right)} \quad D_m = \frac{\Gamma\left(1+\frac{4}{\mu}\right)}{\Lambda\Gamma(1+\frac{3}{\mu})}$$

$$D_{\mathrm{med}} = \frac{\ln(2)^{\frac{1}{\mu}}}{\Lambda} \quad D_0\text{: no closed-form expression}$$

Fluxes:

$$R \approx 6\pi 10^{-4} a_V N_T \frac{\Gamma\left(1+\frac{3+b_V}{\mu}\right)}{\Lambda^{3+b_V}} \approx 0.0071 N_T \frac{\Gamma\left(1+\frac{3.67}{\mu}\right)}{\Lambda^{3.67}}$$

$$U \approx \frac{\pi}{12} \rho_W 10^{-6} a_V^3 N_T \frac{\Gamma\left(1+\frac{3+3b_V}{\mu}\right)}{\Lambda^{3+3b_V}} \approx 14.12 \cdot 10^{-6} N_T \frac{\Gamma\left(1+\frac{5.01}{\mu}\right)}{\Lambda^{5.01}}$$

Notes: when $\mu = 1$, the distribution reduces to an exponential.

6.4 Normalized DSD models

DSD normalization is a useful technique that makes it possible to analyze and compare the shape of two DSDs that do not have the same moments or characteristic drop diameters [108,109]. The idea behind normalization is that most DSDs look rather similar to each other in terms of their shape, which means it should be possible to approximate them with the help of a single template distribution and a few key moments (e.g., N_T, LWC, Z), allowing most of the DSD variabilities to be explained by variation in the chosen key moments. This hypothesis is supported by empirically observed power-law dependencies between different moments of the DSD, such as in Z–R, D_0–R, and LWC–R relationships [47,73,96,110], and through theoretical arguments, such as the existence of "equilibrium DSDs" in microphysical simulations, in which drop coalescence is perfectly balanced out by drop breakup [86,88].

Generally speaking, the two main approaches to normalization are: (a) methods that assume a functional form for the DSD, such as an exponential or gamma distribution and (b) methods that do not impose any functional form. The earliest attempts at normalization assumed fixed parametric DSD shapes and used a single normalizing factor such as the concentration parameter N_0, median volume diameter D_0, or exponential slope Λ [25,73]. In the well-known single-normalization of Sempere Torres *et al*. [111], the rain rate (roughly the 3.67th-order moment of the DSD) raised to a fixed power acts as a scaling function for the drop size. However, it was soon discovered that a single moment and template distribution are, in general, insufficient to fully capture all the natural variability of DSDs, with different templates required for stratiform and convective rain [112]. At least a second moment was necessary to reduce the scatter and collapse the observed distributions into a single, compact form. As a result, more general DSD normalization procedures that involve two, three, or more moments and do not make any assumptions about the functional form of the DSD shape were developed [104,109,113,114]. Figure 6.4 shows an example of varying DSDs being "collapsed" into less variable forms by the double-moment normalization of Lee *et al*. [104].

Normalization starts with the observation that from a mathematical point of view, any DSD is uniquely defined by the (infinite) sequence of its statistical moments M_0, M_1, M_2, ... Normalization assumes that only a handful of these moments are necessary to approximate all the others and, consequently, the entire distribution. For example M_3 and M_4 were used by [108], while M_2, M_3, and M_4 were used by [113], and M_0, M_1, M_2, and M_3 by [115]. How many moments to use, their orders, and how to combine them when expressing DSDs is still up for debate, and different combinations are possible depending on the application. However, not all combinations are equally good [116]. The science behind normalization is not yet settled and more research is needed to fully understand the consequences of choosing one approach over another.

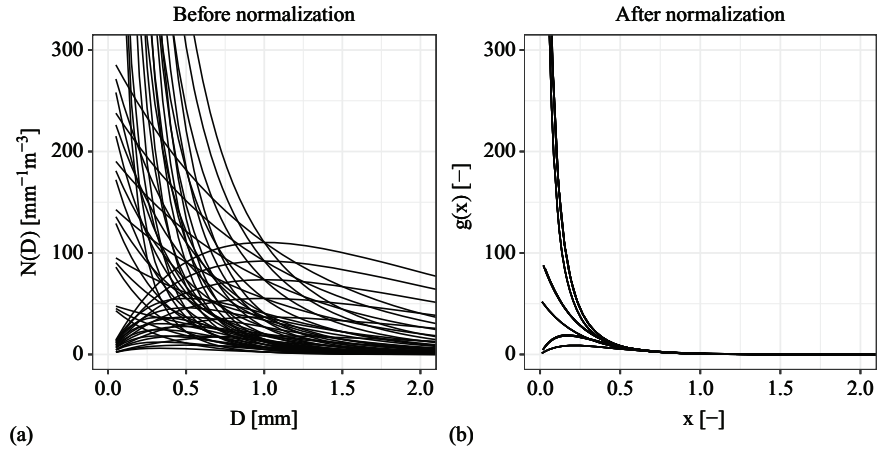

Figure 6.4 An example of the "collapsing" effect of DSD normalization. Panel (a) shows gamma DSDs with varying parameters (N_0 from 50 to 300 in steps of 50, μ equal to -1, 0, or 1, and Λ equal to 1, 2, or 3). Panel (b) shows the double-moment normalized [104] versions of the same DSDs, with $g(x) = N(D)/\left(M_i^{(j+1)/(j-i)} M_j^{(i+1)/(i-j)}\right)$, $x = DM_i^{1/(j-i)} M_j^{-1/(j-i)}$ and $i = 3$ and $j = 6$. The normalized DSDs clearly exhibit much lower variability compared to the original ones.

The most straightforward way to build a normalized DSD model is to divide the drop size D in (6.1) by a characteristic drop diameter D_c (mm) to render it dimensionless [117]. This leads to

$$N(D) = N_c g\left(\frac{D}{D_c}\right), \tag{6.19}$$

where N_c (mm^{-1} m^{-3}) is a characteristic number concentration that depends on the choice of D_c and g is a distribution function called the "template distribution." Using this notation, and setting $x = \frac{D}{D_c}$ (-), the moments of the normalized DSD are

$$M_n = N_c D_c^{n+1} \int_x x^n g(x) dx = N_c D_c^{n+1} \xi_n, \tag{6.20}$$

where

$$\xi_n = \int_x x^n g(x) dx. \tag{6.21}$$

Next, we choose a reference moment M_i of interest and express the characteristic number concentration N_c as a function of it, such that

$$N_c = \frac{M_i}{D_c^{i+1}} \xi_i^{-1}. \tag{6.22}$$

This expression leads to a normalized DSD for a given reference moment M_i, characteristic drop diameter D_c, and distribution g:

$$N(D) = \frac{M_i}{D_c^{i+1}} \xi_i^{-1} g\left(\frac{D}{D_c}\right). \tag{6.23}$$

The characteristic diameter D_c can be the mean drop diameter D_{mean}, the median volume diameter D_0, the mass-weighted mean drop diameter D_m, or any other quantity that has units of mm. The reference moment can be the drop concentration (M_0), liquid water content (M_3), reflectivity (M_6), or any other moment of interest. The template distribution can be a simple parametric model (e.g., exponential, gamma) or any non-parametric model that fits the data. In some formulations [104], the template g is chosen such that $\xi_i = 1$, which simplifies the expression for N_c in (6.22). The downside of this approach is that it is slightly less general, since it makes the template function dependent on choice of the reference moment M_i.

One important consequence of (6.22) is that the characteristic drop diameter D_c must be a power law of the reference moment M_i.

$$D_c = \left(\frac{M_i}{N_c \xi_i}\right)^{\frac{1}{i+1}} \tag{6.24}$$

Equations (6.19)–(6.24) form the mathematical basis for understanding single-moment and multiple-moment normalization techniques. For example, in the single-moment normalization framework by [111], the characteristic drop size is $D_c = M_i^{\beta}$, which leads to $N_c = M_i^{1-\beta(i+1)} \xi_i^{-1} = M_i^{\alpha}$ where $\alpha = 1 - \beta(i+1) - \dfrac{\ln(\xi_i)}{\ln(M_i)}$. More generally, if we assume that the characteristic drop diameter $D_c = \left(\frac{M_j}{M_i}\right)^{\frac{1}{j-i}}$ depends on two reference moments M_i and M_j, we get the double-moment normalization framework of Lee *et al.* [104].

The flashcards on the next pages summarize the most common normalization frameworks and provide some examples of special cases that are worth mentioning. In an effort to be as consistent as possible and use common notations throughout the chapter, we had to make some small changes to the notations commonly used in the literature. For example, we use $g()$ to denote any generic template function, ξ_n for the nth-order moment of the template function, D_c for the characteristic drop size, and N_c for the intercept parameter, notwithstanding that in particular formulations and publications, the specific definitions and notations of $g()$, ξ_n, N_c, and D_c can change. For example, in the double-moment normalization framework, the template function is often denoted as $h()$.

Single-moment normalization

$$N(D) = M_i^{\alpha} g(M_i^{-\beta} D) = N_c g\left(\frac{D}{D_c}\right)$$

Explanations: The DSD is written as a function of a generic shape function g, a single reference moment M_i, and two scaling coefficients $\alpha, \beta \in \mathbb{R}$ [111,118]. The variable $x = M_i^{-\beta} D$ is a single-normalized drop diameter. The shape function g can be empirical (parameter free), or any parametric model.

Moments:

$$M_n = M_i^{\alpha+\beta(n+1)} \xi_n \frac{M_n}{M_m} = M_i^{\beta(n-m)} \frac{\xi_n}{\xi_m}$$

where $\xi_n = \int_0^{\infty} x^n g(x) dx$.
Self-consistency constraint: $\alpha + \beta(i+1) = 1$ (assuming $\xi_i = 1$)

Property: All moments of the DSD are linked through a power law:

$$M_n = a(n, m, i, \beta) M_m^{b(n,m,i,\beta)}$$

with $b(n, m, i, \beta) = \dfrac{1 + \beta(n-i)}{1 + \beta(m-i)}$ and $a(n, m, i, \beta) = \dfrac{\xi_n}{\xi_m^{b(n,m,i,\beta)}}$.
State variables:

$$N_T = M_i^{\alpha+\beta} \xi_0 \quad \text{LWC} = \frac{\pi \rho_W}{6000} M_i^{\alpha+4\beta} \xi_3 \quad Z = M_i^{\alpha+7\beta} \xi_6$$

Characteristic sizes:

$$D_{\text{mean}} = M_i^{\beta} \frac{\xi_1}{\xi_0} \quad D_a = M_i^{\beta} \frac{\xi_3}{\xi_2} \quad D_m = M_i^{\beta} \frac{\xi_4}{\xi_3}$$

Notes: the special case $i = 3.67$ leads to the original formulation [111] in which the normalizing variable is the rain rate R:

$$N(D) = R^{\alpha} g(R^{-\beta} D)$$

with $\alpha + 4.67\beta = 1$ and $Z = \xi_6 R^{1+2.33\beta}$. The limiting case where $\alpha = 1$ and $\beta = 0$ leads to a number-controlled equilibrium DSD [88] in which $N(D) = M_i g(D)$ and $Z = \dfrac{\xi_n}{\xi_m} R$.

Double-moment normalization

$$N(D) = M_i^{(j+1)(j-i)} M_j^{(i+1)(i-j)} g\left(\frac{D}{D_c}\right) = N_c\, g\left(\frac{D}{D_c}\right)$$

with $D_c = \left(\frac{M_j}{M_i}\right)^{\frac{1}{j-i}}$ and $N_c = M_i^{(j+1)(j-i)} M_j^{(i+1)(i-j)}$.

Explanations: The DSD is written as a combination of a generic shape function $g()$, concentration N_c and double-moment normalized drop diameter D_c [104]. The normalizing moments i and j do not necessarily need to be consecutive. The two-moment normalization schemes capture more variability in slope and intercept than single-moment normalization at the expense of a higher number of parameters and higher model complexity.

Moments:

$$M_n = N_c D_c^{n+1} \xi_n \quad \text{where} \quad \xi_n = \int_0^\infty x^n g(x) dx$$

Self-consistency constraints: $\xi_i = \xi_j = 1$

Property: All moments are linked to each other through a power-law:

$$M_n = N_c^{\frac{m-n}{m+1}} M_m^{\frac{n+1}{m+1}} \xi_n \xi_m^{\frac{-(n+1)}{m+1}}.$$

The relationship above is independent of the shape of the DSD and forms the theoretical justification for the observed power-law relationship between different moments of the DSD, such as reflectivity and rain rate [108].

Characteristic sizes:

$$D_{\text{mean}} = D_c \frac{\xi_1}{\xi_0} \quad D_a = D_c \frac{\xi_3}{\xi_2} \quad D_m = D_c \frac{\xi_4}{\xi_3}$$

Notes: when $i = 3$ and $j = 4$, we have $D_c = D_m$ and $N_c = M_3^5 M_4^{-4} = M_3 D_m^{-4}$ which leads to the original formulation proposed by [108]. Studies show that around 80% of the DSD variability can be captured using two moments [114]. Moreover, $g(x)$ can reasonably be assumed static for practical purposes, at least in stratiform rain, with some important caveats [116]. However, a single template function remains insufficient to fully capture all the small-scale variability in the DSD, such as the formation of bi-modal distributions [113,119].

General N-moment normalization

$$f(D) = N_c g\left(\frac{D}{D_c}\right)$$

where D_c is a characteristic drop size that is a function of N different moments of $N(D)$, and N_c is a normalized intercept [114] as in (6.22).

Moments: Any moment M_n is approximated by a power-series with J terms using N normalizing moments $M_{i_1}, \ldots, M_{i_N}$, such that

$$M_n \approx \begin{cases} \sum_{j=1}^{J} a_{jn} \prod_{k=1}^{N-1} \left(\frac{M_{i_{k+1}}}{M_{i_k}}\right)^{b_{kjn}} & \text{if } N \geq 2 \\ \sum_{j=1}^{J} a_{jn} M_i^{b_{jn}} & \text{if } N = 1 \end{cases}$$

where a_{jn} and b_{kjn} are estimated from the data. $J = 1$ is often chosen since otherwise estimating optimal coefficients is complicated. For $J = 1$, we have:

$$M_n \approx \begin{cases} a_n \prod_{k=1}^{N-1} \left(\frac{M_{i_{k+1}}}{M_{i_k}}\right)^{b_{kn}} & \text{if } N \geq 2 \\ a_n M_i^{b_n} & \text{if } N = 1 \end{cases}.$$

Characteristic drop sizes: the dimensional constraints needed to derive expressions for D_c for any value of N are available [114]. For $N \geq 3$, there are multiple ways to define D_c that lead to dimensional consistency.

$N = 1$	$N = 2$	$N = 3$
$D_c \propto M_{i_1}^{\frac{1}{i_1 - 3}}$	$D_c \propto \left(\frac{M_{i_2}}{M_{i_1}}\right)^{\frac{1}{i_2 - i_1}}$	$D_c \propto \left(\frac{M_{i_1}}{M_{i_3}} \frac{M_{i_2}}{M_{i_3}}\right)^{\frac{1}{i_1 - 2i_2 + i_3}}$

More generally, for any even value of N, with $N \geq 4$, we have:

$$D_c \propto \prod_{k=1}^{N/2} M_{i_{2k-1}}^{\frac{1}{c}} \prod_{k=1}^{N/2} M_{i_{2k}}^{-\frac{1}{c}} \text{ with } c = \sum_{k=1}^{N/2} i_{2k-1} - \sum_{k=1}^{N/2} i_{2k}.$$

For every odd value of N with $N \geq 5$, we have:

$$D_c \propto \prod_{k=1}^{\frac{1}{2}(N-1)} M_{i_{2k-1}}^{\frac{1}{c}} \prod_{k=1}^{\frac{1}{2}(N-3)} M_{i_{2k}}^{-\frac{1}{c}} M_{i_{N-1}}^{-2/c} \text{ with } c = \sum_{k=1}^{\frac{1}{2}(N-1)} i_{2k-1} - \sum_{k=1}^{\frac{1}{2}(N-3)} i_{2k} - 2i_{N-1}.$$

6.4.1 Particular cases in DSD normalization

In this section, we highlight some particular cases for single-moment, double-moment, and N-moment normalization.

6.4.1.1 Single-moment normalization

In single-moment normalization [111], special cases arise when the template distribution used is the exponential model or gamma model.

Exponential model: if the template distribution is the exponential model, such that $g(x) = N_0 \exp(-\Lambda x)$, the self-consistency constraint implies that

$$N_0 = \frac{\Lambda^{i+1}}{\Gamma(i+1)}, \tag{6.25}$$

and therefore the normalized DSD is

$$N(D) = M_i^{\alpha} \frac{\Lambda^{i+1}}{\Gamma(i+1)} \exp\left(-\Lambda M_i^{-\beta} D\right). \tag{6.26}$$

This equation means that the single-moment normalized version of an exponential DSD is an exponential in which the concentration parameter is fully determined by the slope Λ of the template distribution, the reference moment M_i and the scaling exponent β.

Gamma model: if the template distribution is the gamma model, such that $g(x) = N_0 x^{\mu} \exp(-\Lambda x)$, then the self-consistency constraint implies that

$$N_0 = \frac{\Lambda^{\mu+i+1}}{\Gamma(\mu+i+1)}, \tag{6.27}$$

and the normalized DSD is

$$N(D) = M_i^{\alpha} \frac{\Lambda^{\mu+i+1}}{\Gamma(\mu+i+1)} \left(M_i^{-\beta} D\right)^{\mu} \exp\left(-\Lambda M_i^{-\beta} D\right), \tag{6.28}$$

which is another gamma distribution where the concentration parameter depends on the reference moment M_i, power β, and slope Λ.

6.4.1.2 Double-moment normalization

In double-moment normalization [104], special cases arise when the template distribution is the exponential, gamma, and generalized gamma.

Exponential model: if $g(x) = N_0 \exp(-\Lambda x)$, the self-consistency constraint $\xi_i = \xi_j = 1$ implies that

$$\Lambda = \left(\frac{\Gamma(j+1)}{\Gamma(i+1)}\right)^{\frac{1}{j-i}} \text{ and } N_0 = \frac{\Lambda^{i+1}}{\Gamma(i+1)},$$

and the normalized DSD is:

$$N(D) = \frac{N_c}{\Gamma(i+1)} \left(\frac{\Gamma(j+1)}{\Gamma(i+1)} \right)^{\frac{i+1}{j-i}} \exp\left[-\left(\frac{\Gamma(j+1)}{\Gamma(i+1)} \right)^{\frac{1}{j-i}} \frac{D}{D_c} \right]. \tag{6.29}$$

In particular, if $i = 3$ and $j = 4$, we get $D_c = D_m$ and $N_c = M_3^5 M_4^{-4} = M_3 D_m^{-4}$ and

$$N(D) = \frac{M_3}{6D_m^4} 4^4 \exp\left(-4\frac{D}{D_m} \right) = 256 \cdot 10^3 \frac{\text{LWC}}{\pi \rho_W D_m^4} \exp\left(-4\frac{D}{D_m} \right), \tag{6.30}$$

$$N(D) = N_w \exp\left(-4\frac{D}{D_m} \right), \tag{6.31}$$

with

$$N_w = 256 \cdot 10^3 \frac{\text{LWC}}{\pi \rho_W D_m^4}. \tag{6.32}$$

Gamma model: if $g(x) = N_0 x^\mu \exp(-\Lambda x)$, the self-consistency constraint implies

$$\Lambda = \left(\frac{\Gamma(\mu + j + 1)}{\Gamma(\mu + i + 1)} \right)^{\frac{1}{j-i}} \text{ and } N_0 = \frac{\Lambda^{\mu+i+1}}{\Gamma(\mu + i + 1)},$$

and the double-moment normalized gamma DSD is

$$N(D) = N_c N_0 \left(\frac{D}{D_c} \right)^\mu \exp\left[-\left(\frac{\Gamma(\mu + j + 1)}{\Gamma(\mu + i + 1)} \right)^{\frac{1}{j-i}} \frac{D}{D_c} \right]. \tag{6.33}$$

In particular, if $i = 3, j = 4$, and $D_c = D_m$, we get $\Lambda = \dfrac{\Gamma(\mu + 5)}{\Gamma(\mu + 4)} = \mu + 4$ and

$$N(D) = N_w f(\mu) \left(\frac{D}{D_m} \right)^\mu \exp\left[-(\mu + 4)\frac{D}{D_m} \right], \tag{6.34}$$

with N_w as in (6.32) and

$$f(\mu) = \frac{6}{256} \frac{(\mu + 4)^{\mu+4}}{\Gamma(\mu + 4)}. \tag{6.35}$$

These equations for the double-normalized DSD with the gamma and exponential models show that the intercept parameter N_w of a double-normalized gamma DSD with $i = 3$ and $j = 4$ can be interpreted as the concentration of a double-moment normalized exponential DSD with similar liquid water content [25,104,108]. The clear physical interpretation of N_w and the fact that its units do not depend on μ are why it is usually preferred over N_0 [48]. Moreover, studies have shown that N_w varies by "only" approximately 3–4 orders of magnitude compared with the 6–7 orders of magnitude for N_0 [85,108]. Since normalization by $D_c = D_m$ is the most common in the literature, (6.34) is often referred to as "the normalized gamma model" [108,120,121]. It is widely used in the ground-based radar and satellite remote-sensing communities and, notably, has been adopted by the Global Precipitation Measurement (GPM) Dual-Frequency Precipitation Radar (DPR) algorithm [84,122,123].

Generalized gamma model: if we have

$$g(x) = \frac{N_T}{\Gamma\left(\frac{\mu+1}{c}\right)} c\Lambda^{\mu+1} x^{\mu} \exp\left[-(\Lambda x)^c\right],$$

and $\xi_i = \xi_j = 1$ then we must have

$$\Lambda = \left[\frac{\Gamma\left(\frac{\mu+1+j}{c}\right)}{\Gamma\left(\frac{\mu+1+i}{c}\right)}\right]^{\frac{1}{j-i}} \text{ and } N_T = \frac{\Gamma\left(\frac{\mu+1}{c}\right)}{\Gamma\left(\frac{\mu+1+i}{c}\right)} \Lambda^i.$$

Therefore, the normalized DSD is

$$N(D) = \frac{cN_c}{\Gamma\left(\frac{\mu+1+i}{c}\right)} \left[\frac{\Gamma\left(\frac{\mu+1+j}{c}\right)}{\Gamma\left(\frac{\mu+1+i}{c}\right)}\right]^{\frac{\mu+i+1}{j-i}} \left(\frac{D}{D_c}\right)^{\mu} \exp\left\{-\left[\frac{\Gamma\left(\frac{\mu+1+j}{c}\right)}{\Gamma\left(\frac{\mu+1+i}{c}\right)}\right]^{\frac{c}{j-i}} \left(\frac{D}{D_c}\right)^{c}\right\} \tag{6.36}$$

In particular, if $i = 3$ and $j = 4$, we get:

$$N(D) = \frac{cM_3}{D_m^4 \Gamma\left(\frac{\mu+4}{c}\right)} \left[\frac{\Gamma\left(\frac{\mu+5}{c}\right)}{\Gamma\left(\frac{\mu+4}{c}\right)}\right]^{\mu+4} \left(\frac{D}{D_m}\right)^{\mu} \exp\left\{-\left[\frac{\Gamma\left(\frac{\mu+5}{c}\right) D}{\Gamma\left(\frac{\mu+4}{c}\right) D_m}\right]^{c}\right\}. \tag{6.37}$$

6.4.1.3 General *N*-moment normalization

Special cases in general N-moment normalization involve specific values of N, the number of normalizing moments, while the number of terms in the power series is kept at $J = 1$ [114].

N = 1 and J = 1: if a single moment $M_{i_1} = M_i$ is known, then $D_c = cM_i^{\frac{1}{i-3}}$, where $c \in \mathbb{R}$ is some constant. To have equivalence with the single-normalization framework in which $D_c = M_i^{\beta}$, one must have $c = M_i^{\beta - \frac{1}{i-3}}$. Moreover, any moment M_n will be approximately related to the reference moment M_i by a power law of the form $M_n \approx a_n M_i^{b_n}$. This is very similar to the single-moment normalization framework in which $M_n = \frac{\xi_n}{\xi_i^{1+\beta(n-i)}} M_i^{1+\beta(n-i)}$. In fact, the two frameworks will be perfectly equivalent if a_n and b_n are chosen such that $a_n = \frac{\xi_n}{\xi_i^{1+\beta(n-i)}} M_i^{1+\beta(n-i)-b_n}$. The main difference is that in the general N-moment normalization framework, the parameters a_n and b_n are fitted to the data instead of being determined by the reference moment, which means that the constraint above might not necessarily be satisfied.

N = 2 and J = 1: if two moments $M_{i_1} = M_i$ and $M_{i_2} = M_j$ are known, the characteristic drop size is

$$D_c = \left(\frac{M_{i_2}}{M_{i_1}}\right)^{\frac{1}{i_2 - i_1}},$$

and

$$M_n = a_n \left(\frac{M_{i_2}}{M_{i_1}}\right)^{b_n} = a_n D_c^{b_n(j-i)},$$

which is identical to the two-moment normalization if $a_n = N_c \xi_n \left(\frac{M_j}{M_i}\right)^{\frac{n+1}{j-i} - b_n}$.

N = 3 and J = 1: if three moments M_{i_1}, M_{i_2} and M_{i_3} are known, we have

$$D_c = \left(\frac{M_{i_1}}{M_{i_3}} \frac{M_{i_2}}{M_{i_3}}\right)^{\frac{1}{i_1 - 2i_2 + i_3}},$$

and

$$M_n = a_n \left(\frac{M_{i_2}}{M_{i_1}}\right)^{b_{1n}} \left(\frac{M_{i_3}}{M_{i_2}}\right)^{b_{2n}} = a_n M_{i_1}^{1-b_{1n}} M_{i_2}^{b_{1n}-b_{2n}} M_{i_3}^{b_{2n}}.$$

6.5 DSDs and weather radar

The DSD provides statistical information about the raindrops contained in a volume of air, and consequently, about the targets illuminated by a radar beam. Therefore, the DSD plays a key role in weather radar. In this section, we briefly review how the DSD influences quantitative rainfall estimation in weather radar and how the additional information provided by polarimetric and Doppler radar can be used to estimate DSDs. This section is intended to be a brief summary rather than an exhaustive review of the existing literature on the topic.

6.5.1 Radar variables

In the early days, weather radars mostly consisted of single-polarization, single-frequency systems. The main variable associated to such a conventional system is the radar reflectivity factor Z, as defined in (6.7). If the radar has Doppler capability, the mean Doppler velocity, its standard deviation and possibly the full Doppler spectrum can also be used to provide information about radial wind speeds. Nowadays, many weather radars have polarimetric (i.e., dual-polarization and Doppler) capabilities, collecting additional radar variables that can be used for rainfall estimation and DSD retrieval. Below, the most common variables provided by a single-frequency, polarimetric weather radar are listed, together with their expressions as a function of the DSD. For a more detailed description of polarimetric radar, the reader is referred to [48,85].

Radar reflectivity at horizontal/vertical polarization

Equation (6.7) provides the theoretical reflectivity factor Z in the Rayleigh limit associated with a given DSD. However, in the general case (i.e., including the non-Rayleigh scattering regimes), the radar reflectivity at horizontal (Z_h) and vertical (Z_v) polarizations (in mm^6m^{-3}) are defined as:

$$Z_h = 10^6 \frac{\lambda^4}{\pi^5 |K|^2} \int_0^\infty \sigma_{bh}(D) N(D) dD, \tag{6.38}$$

and

$$Z_v = 10^6 \frac{\lambda^4}{\pi^5 |K|^2} \int_0^\infty \sigma_{bv}(D) N(D) dD. \tag{6.39}$$

where λ (cm) is the radar signal wavelength, K (–) is the dielectric factor and $\sigma_{bh}(D)$ and $\sigma_{bv}(D)$ (cm^2) are the backscattering cross sections of a drop of diameter D at horizontal and vertical polarizations (e.g. [48,85]).

Note that in the Rayleigh regime, $\sigma_{bh/v}(D)$ is proportional to $\frac{D^6}{\lambda^4}$ with a factor related to the non-sphericity of raindrops [85, Equation (5.1)], which makes the above equation consistent with (6.7).

Differential radar reflectivity

The differential radar reflectivity Z_{DR} (dB) is defined as

$$Z_{DR} = 10 \log_{10} \left(\frac{Z_h}{Z_v} \right) = 10 \log_{10} \left(\frac{\int_0^\infty \sigma_{bh}(D) N(D) dD}{\int_0^\infty \sigma_{bv}(D) N(D) dD} \right). \tag{6.40}$$

Since $N(D) = N_T f(D)$, the differential reflectivity depends on the shape of the DSD, but not on the number concentration of drops. At non-vertical incidence angles, Z_{DR} is positive for oblate particles such as raindrops, negative for prolate particles, and zero for spherical particles. This makes it a very useful variable for retrieving information about the (reflectivity-weighted) axis ratio of raindrops, characteristic drop sizes and orientations [124].

Copolar cross-correlation coefficient

The copolar cross-correlation coefficient ρ_{hv} (–) is defined as

$$\rho_{hv} = \left| \frac{\int_0^\infty S_{hh}^*(D) S_{vv}(D) N(D) dD}{\left[\int_0^\infty S_{hh}^2(D) N(D) dD \int_0^\infty S_{vv}^2(D) N(D) dD \right]^{0.5}} \right|, \tag{6.41}$$

where $S_{hh}(D)$ and $S_{vv}(D)$ (cm) denote the backscattering amplitudes in the horizontal/vertical polarization and * is the complex conjugate operator.

Although ρ_{hv} is not directly related to rainfall estimation, it is sensitive to particle axis ratio and shapes and can therefore be very useful for identifying regions with mixed precipitation types, such as a combination of rain and ice [125]. Low values of ρ_{hv} are often indicative of heterogeneous hydrometeor types in the sampling volume, or the presence of non-meteorological scatterers.

Specific differential phase shift

The specific differential phase shift on propagation K_{dp} ($^\circ$km^{-1}) is defined as

$$K_{dp} = \frac{18\lambda}{\pi} \int_0^\infty \Re[F_{hh}(D) - F_{vv}(D)]N(D)dD \tag{6.42}$$

where $\Re[F_{hh/vv}(D)]$ (cm) denotes the real part of the forward scattering amplitude in the horizontal(vertical) polarization [48].

The specific differential phase shift K_{dp} is influenced by the concentration, shape, and orientation of drops. Because K_{dp} is retrieved from a phase measurement, it has several interesting advantages over amplitude measurements, including a higher immunity to additive noise [126]. Compared to reflectivity, K_{dp}, therefore, tends to be relatively unaffected by radar miscalibration, attenuation, and partial beam blockage. The main disadvantage is that calculating K_{dp} requires significant signal processing and spatial averaging to filter out noise, which can be challenging in low-to-moderate intensity precipitation (due to limited phase variations).

6.5.2 Rain rate retrieval from radar

The rain rate R (6.10) is a variable of interest for many hydrological and natural hazard applications. Since the early days of weather radar, it has been empirically established that Z (in mm^6 m^{-3}) and R (in mm h^{-1}) appear to be linked by a power law [92], such that

$$Z = aR^b. \tag{6.43}$$

The famous Marshall–Palmer relationship is given by $Z = 200R^{1.6}$ [127]. However, a variety of different values for the prefactor a and exponent b have been proposed in the literature. For example, Battan [47] lists 69 different sets of prefactors and exponents. The different DSD normalization frameworks (see Section 6.4) also contributed to establishing different power law models for linking Z to R. The single-moment normalization framework gives an explicit link between the prefactor a and the sixth-order moment of the normalized DSD template $g(x)$, as well as between the exponent and the normalization parameter β [64]. The double-moment normalization framework generalizes this approach by providing explicit links between the parameters a and b, on

the one hand, and the two chosen reference moments and double-moment-normalized DSD template $g(x)$, on the other hand.

Various rainfall estimation algorithms for polarimetric radar measurements have also been proposed. The literature on this topic is vast and an exhaustive review is beyond the scope of this chapter. The studies by Bringi and Chandrasekar [48] and Chen and Chandrasekar [128] provide a good overview of the most common techniques. The latter distinguishes between four main types of (power-law) estimators known as $R(Z_h)$, $R(Z_h, Z_{DR})$, $R(K_{dp})$, and $R(Z_{dr}, K_{dp})$ with each estimator having its own advantages and disadvantages depending on rain rate, type of rain, radar resolution, calibration, and measurement uncertainties. For example, at X-band, Z_h and Z_{DR} are known to be severely affected by attenuation which makes K_{dp} a good choice for estimating rainfall rates in heavy rain. In light rain, on the other hand, Z_{DR} and K_{dp} will be of little use for rain rate estimation as they approach zero.

6.5.3 DSD retrieval from radar

Thanks to the additional variables provided by polarimetric radars, it becomes possible to retrieve information about the DSD in the atmosphere. Retrievals based on the reflectivity factor at horizontal polarization, differential reflectivity, and specific differential phase are the most common choices because of their natural links to raindrop concentrations, sizes, and shapes. However, since the number of available independent radar variables is limited, relatively simple parametric DSD models with two or three degrees of freedom must be assumed (see Section 6.3.1). For example, if the exponential distribution is used, N_0 and Λ can be retrieved from Z_{hh} and Z_{DR} [9,124]. Zhang *et al*. [102] proposed a retrieval based on two moments Z_h and Z_{DR} and a gamma DSD model where μ and Λ are constrained by a deterministic relationship. However, similar to the Z–R relationship, μ–Λ relationships are known to fluctuate with rainfall type and climatology [129,130], which adds additional uncertainty and modeling errors during the retrievals. Alternatively, N_0, μ and Λ can be obtained directly from Z_h, Z_{DR} and K_{dp} by solving a system of three nonlinear equations. Three-parameter retrieval methods based on Z_h and Z_{DR} and K_{dp} exist for the normalized gamma model [82,120] and for the double-moment normalization based on a generalized gamma distribution [131,132]. Methods that use Z_{DR} or K_{dp} must contend with noise in these variables during light rain [120,131,133].

According to Huang *et al*. [134], there has not yet been any comprehensive study about the added value of including K_{dp} in DSD retrievals. One of the challenges in retrieving DSDs from polarimetric radar is that most radar quantities relate to high-order moments of the DSD (e.g., 4.6 for K_{dp} and 6 for Z) [132], which introduces a lot of uncertainties for the lower-order moments. Z_{DR} is an exception to this because it relates to a characteristic size (i.e., the ratio between the seventh- and the sixth-order moment [132]) and is, therefore, independent of concentration. However, because it involves two high-order moments and is difficult to measure and calibrate accurately, Z_{DR} often cannot be used to precisely retrieve the lower-order moments of the DSD either. Nevertheless, progress has been made in lower-order moment estimation

through the use of climatological parameters for the generalized gamma distribution used with the double-moment normalized DSD [132].

In recent years, several interesting data-driven retrieval methods based on machine learning or non-linear mappings between radar observables and DSDs have also been proposed [135–139]. These methods, when combined with estimates of natural variations for a given input, can provide non-parametric, probabilistic DSD retrievals and associated confidence intervals. Data-driven methods are an intriguing alternative to parametric DSD retrievals as they make fewer (or different) modeling assumptions and can handle the non-linearity of the involved equations at a relatively low computational cost. However, they require large amounts of data for proper training and suffer from the same intrinsic limitations as parametric methods (i.e., limited information about low-order moments in radar observations and large measurement uncertainties).

The Doppler spectra obtained from vertically pointing radars also provide valuable information on the size, shape, and fall velocity of precipitating particles, which can be used to retrieve the raindrop size distribution. Several DSD retrieval methods for vertically pointing radars at various frequencies have been developed and evaluated [60,140,141]. Most retrieval methods exploit the fact that the terminal velocities of raindrops tend to be well constrained by their diameters (see (6.8)). The shape and width of the Doppler spectrum (i.e., the distribution of spectral reflectivity as a function of the radial velocity) at vertical incidence can, therefore, be used to retrieve empirical drop size distributions. The method assumes negligible (or known) vertical wind speeds, and limited turbulence.

Finally, it should be mentioned that other, more elaborate DSD retrieval methods that require special types of radars or measurements have been proposed, such as double frequency [142], triple frequency [143], and/or Doppler power spectra [144]. These methods go beyond the scope of this chapter.

6.6 DSDs in numerical weather prediction models

Atmospheric models such as those used for numerical weather prediction (NWP) are run at application-specific spatial resolution, which is referred to as the grid spacing. Atmospheric processes that occur on scales smaller than the grid spacing are called "sub-grid" processes, and their effects must be accounted for using a modelling scheme that parameterizes the process effects. For example, most atmospheric models are run at grid spacings at which individual convective cells are not resolved; yet the sub-grid effects of convection are important and must be parameterized using a convection scheme [145,146]. Likewise, microphysics schemes parameterize the status and physical effects of particles present in the atmosphere, such as cloud particles, raindrops, and snowflakes. While recent increases in computing power have allowed for some processes, like convection, to sometimes be explicitly modeled without the use of parameterizations, microphysics schemes are still required for NWP, simply because there are far too many particles in the atmosphere to explicitly model them all with available computational power [147].

Microphysics schemes use models of the size distributions for the different types of particles they represent, including for representing the DSD and correspondingly the rain properties in the model. The job of a microphysics scheme is to keep track of these particle size distributions and use "process rate equations" to determine how the size distributions change in response to physical processes [147]. For the DSD, these processes include drop coalescence, collisions, evaporation, and drop breakup [17,147]. In this section, we briefly discuss some of the broad issues surrounding treatment of DSDs in model microphysics schemes, citing just some of the many specific scheme implementations that are available. For a more complete examination, the reader is referred to recent reviews [147–149].

Microphysical parameterizations can be broadly divided into *bulk*, *bin*, and *Lagrangian* schemes. The majority of microphysical parameterizations today are bulk schemes [148,150], in which the DSD is represented by a small number of key DSD moments that describe bulk DSD properties, such as drop mass or number, and the DSD is assumed to follow a simple parametric form such as the exponential or Gamma distribution, the properties of which depend on the values of the chosen DSD moments [147]. The first such schemes were "one-moment," in that they modeled DSDs using predictions of a variable related to a single DSD moment, typically the particle mass which is proportional to the third-order moment [147]. In one-moment schemes [150–152], other DSD model components, such as number concentration, are kept fixed. As an example, in a scheme that uses the exponential DSD model, it is common to allow the slope parameter to vary while assuming a constant concentration parameter [151]. One-moment schemes are computationally efficient, but contain strong assumptions that can introduce errors into DSD representations [153]. More complex "two-moment" schemes [154–157] use predictions of two quantities, typically the particle mass and particle concentration, and allow for more realistic DSD parameterization [147,149,153]. More recent schemes use predictions of three [158–162] and even five [163] moments.

In contrast to bulk schemes, spectral or bin microphysics parameterizations [164,165] explicitly model the DSD using discrete bins of raindrop size. Bin schemes are computationally expensive and mostly used for idealized studies of microphysical processes [147,148]. Because they are assumed to have less uncertainty than bulk schemes, bin microphysics schemes are often used to provide benchmark results with which to test other schemes [166,167]. However, it should be noted that given the difficulty in actually observing microphysical processes for comparison with bin or bulk schemes, there is a lack of evidence that bin schemes consistently perform better than bulk schemes [147]. A third and more recently developed scheme type is Lagrangian microphysics schemes [168,169], in which "super particles" that represent a population of actual particles are followed through the flow while their properties, including their number, are tracked; sampling from these super particles can then provide an estimate of the DSD [147]. Lagrangian schemes have similar computational expense as bin schemes [147,170], but have the advantage over bin schemes that they are not affected by "broadening" of particle distributions caused by numerical diffusion [171]. Overall, the choice of which microphysics scheme type and complexity to

use is heavily dependent on the fidelity required for the application and the available computational power.

Microphysics process rate equations are used to represent modeled microphysical processes. The equations used depend on the type of scheme, but, in all cases, the rates depend on particle size [148]. The main processes that are modeled for the DSD include droplet nucleation, in which drops form around cloud condensation nuclei; droplet growth, which occurs via vapor diffusion and releases latent heat; drop collisions, which can lead to coalescence and drop breakup; and sedimentation, the "falling out" of raindrops [148]. Microphysics schemes are notoriously complex and uncertainties exist in their components, from the representation of particle distributions to the process rate equations [147,148]. For the DSD, a particularly challenging area of uncertainty is the parameterization of raindrop coalescence and breakup [147]. Microphysical uncertainties are compounded by difficulties in observing microphysics processes, whether in the laboratory, in situ, or using remote-sensing techniques such as radar [147]. When it comes to radar, studies that estimate microphysical properties either using polarimetric data [26,131,132,136,172,173] or vertically pointing Doppler radar [174–176] are of particular use in linking observations to specific microphysical processes [177–179] although uncertainties make quantifying process rates from radar data challenging [147].

6.7 Conclusions and future directions

Being able to characterize the number and sizes of raindrops is useful in many fields, including meteorology, hydrology, agriculture, and telecommunications. Drop size distributions, which contain this information, are the result of many different physical processes, including drop coalescence, aggregation, breakup, and evaporation. In the turbulent environment inside a storm, DSDs are constantly changing and evolving, and exhibit great natural variability. DSDs thus come in a wide variety of shapes and forms, and vary from storm to storm, over the duration of a storm, with height, wind properties, and local climatology. No simple model can adequately capture all possible cases and finding the right balance between goodness-of-fit and model complexity can be challenging. In this chapter, we have introduced the DSD and its properties, summarized the most-popular parametric DSD models in use today, discussed normalized DSD models, and given an overview of the use of the DSDs in weather radar and microphysics schemes. While writing this chapter, we identified several outstanding issues related to the measurement, modeling and usage of DSDs in remote sensing and numerical weather prediction. To conclude the chapter, here we briefly summarize our main findings together with some recommendations for future progress on this important subject.

In terms of measurements, it is clear that we need more precise disdrometers capable of accurately measuring DSDs in a unit reference volume, both near the ground and the aloft. These disdrometers should have the ability to measure DSDs at small temporal scales over large sampling resolutions, without restrictions on the lower/upper drop diameter that can be resolved. A large sampling area is needed to

reduce measurement uncertainties during low rainfall rates, ensure that the largest (and rarest) raindrops are sampled as well as possible, and increase the spatial representativeness of DSDs for remote-sensing applications [180]. A high temporal resolution is needed to study microphysical processes and better quantify the space–time variability of rain. The ability to resolve all drop sizes, including very small ones, is crucial for reducing measurement biases and uncertainty when analyzing, fitting and comparing parametric DSD models [22]. In addition to the existing sensors, new 3D video disdrometers capable of directly measuring the DSD in a given volume of air by taking a three-dimensional snapshot should be developed. Directly measuring the DSD inside a volume instead of inferring it from surface measurements is technologically challenging but would be very valuable for remote-sensing applications. Such 3D sensors would provide a more direct and substantially more accurate way to estimate state variables such as number concentrations, liquid water content, and reflectivity without having to make any assumptions about the fall velocities of raindrops. This last point is particularly important, as accurately measuring fall velocities of raindrops at the surface is difficult and, usually, many drops with abnormally small or large fall velocities need to be discarded during data processing [54,181].

In terms of DSD modeling, there are different improvements that can still be made. The first is to consider models that explicitly take into account the lower and upper bounds on the physically possible drop diameters. These bounds have been deliberately ignored in this chapter. However, it is clear that the truncation of the spectrum between $D_{\min}$ and $D_{\max}$ significantly affects the calculation of DSD moments. In addition to being truncated, most disdrometer data also tend to be binned, which further complicates the problem and detrimentally impacts modeling, fitting, and normalization of DSDs. Models that better accommodate these issues should be considered. However, we note that more elaborate and precise models come at the cost of greater mathematical complexity and lower practical usefulness since often, no closed-form solutions will be available. Consequently, such models should only be considered for specific applications where a more detailed description of the DSD is needed. If, on the other hand, the primary goal is to only reproduce a few key bulk quantities such as liquid water content, rainfall rates, or reflectivity factor without consideration for actual DSD shapes, additional complexity may not be necessary or desirable.

In terms of DSD normalization, the open question remains: what is the minimum amount of information (i.e., degrees of freedom) required to adequately describe the natural variability of the DSD? For example, double-moment normalization attempts to approximate any DSD using two of its moments and a template function $g(x)$ which is assumed to be universal and invariant. If this assumption holds, the implications are profound, because then two DSD moments would contain enough information to retrieve the entire DSD and all its moments. Given that some DSD moments are easier to measure than others, this idea is attractive, and it has been tested for retrieval of the DSD from radar data [131,132] and for correcting DSDs measured by instruments that truncate the distribution [24]. However, the assumption requires the template function to be invariant with respect to time, spatial scale, height, type of rain, and so on. While there are encouraging results that suggest the assumption may hold

well enough for practical purposes [116], one has to be aware of the fact that some DSD variability remains uncaptured, even after double-moment normalization [116]. More work is needed to understand and explain the reasons behind this remaining variability, and develop new normalization techniques that are both accurate and practical to implement.

Despite the many advances that have been made in numerical weather modeling, microphysics schemes still sometimes rely on empirical thresholds and simplified assumptions [147,182]. There also remain important gaps in physics knowledge that affect representations of the DSD in weather models; in particular regarding uncertainties in quantifying raindrop coalescence and breakup [147] and in the effects of aerosols [148]. These uncertainties are compounded by the difficulties inherent in observing microphysical processes [147]. Advances in observations of microphysical processes could lead to better-constrained rate equations. The development of new techniques such as Lagrangian approaches to microphysics parameterization and schemes that incorporate a measure of uncertainty should be encouraged [147]. We highlight that the use of DSD normalization in microphysics schemes shows promise [114,183] and should be further investigated.

Acronyms and abbreviations

dB decibels
DPR dual-frequency precipitation radar
DSD drop size distribution
GPM global precipitation measurement (mission)
LWC liquid water content
MP Marshall and Palmer
NWP numerical weather prediction

References

[1] Beard KV and Chuang C. A new model for the equilibrium shape of raindrops. *J Atmos Sci*. 1987;44(3):1509–1524.
[2] Andsager K, Beard KV, and Laird NF. Laboratory measurements of axis ratios for large rain drops. *J Atmos Sci*. 1999;56(15):2673–2683.
[3] Thurai M and Bringi VN. Drop axis ratios from a 2D video disdrometer. *J Atmos Oceanic Technol*. 2005;22(7):966–978.
[4] Bringi VN, Chandrasekar V, Hubbert J, *et al*. Raindrop size distribution in different climatic regimes from disdrometer and dual-polarized radar analysis. *J Atmos Sci*. 2003;60(2):354–365.
[5] Jaffrain J, Studzinski A, and Berne A. A network of disdrometers to quantify the small-scale variability of the raindrop size distribution. *Water Resour Res*. 2011;47:W00H06.

[6] Jameson A, Larsen M, and Kostinski A. On the variability of drop size distributions over areas. *J Atmos Sci*. 2015;72(4):1386–1397.
[7] Raupach TH and Berne A. Small-scale variability of the raindrop size distribution and its effect on areal rainfall retrieval. *J Hydrometeor*. 2016;17:2077–2104.
[8] Atlas D. Optical extinction by rainfall. *J Meteor*. 1953;10:486–488.
[9] Ulbrich CW. Natural variations in the analytical form of the raindrop-size distribution. *J Climate Appl Meteor*. 1983;22(10): 1764–1775.
[10] Wischmeier WH and Smith DD. Rainfall energy and its relationship to soil loss. *Eos, Tran Am Geophys Union*. 1958;39(2):285–291.
[11] Marshall JS, Langille RC, and Palmer WM. Measurement of rainfall by radar. *J Meteor*. 1947;4:186–192.
[12] Mason BJ and Andrews JB. Drop-size distributions from various types of rain. *Q J Roy Meteor Soc*. 1960;86(369):346–353.
[13] Hardy KR. The development of raindrop-size distributions and implications related to the physics of precipitation. *J Atmos Sci*. 1963;20(4): 299–312.
[14] Johnson DB and Beard KV. Oscillation energies of colliding raindrops. *J Atmos Sci*. 1984;41(7):1235–1241.
[15] Meyers MP, Walko RL, Harrington JY, *et al*. New RAMS cloud microphysics parameterization. Part II: the two-moment scheme. *Atmos Res*. 1997;45(1): 3–39.
[16] Ulbrich CW. The effects of drop size distribution truncation on rainfall integral parameters and empirical relations. *J Climate Appl Meteor*. 1985;24(6): 580–590.
[17] Pruppacher HR and Klett JD. *Microphysics of Clouds and Precipitation*. Second revised and expanded ed. Dordrecht: Springer; 2010.
[18] Kinzer GD and Gunn R. The evaporation, temperature and thermal relaxation-time of freely falling waterdrops. *J Atmos Sci*. 1951;8(2):71–83.
[19] Best AC. The evaporation of raindrops. *Q J Roy Meteor Soc*. 1952;78(336): 200–225.
[20] Gatlin PN, Thurai M, Bringi VN, *et al*. Searching for large raindrops: a global summary of two-dimensional video disdrometer observations. *J Appl Meteor Climatol*. 2015;54(5):1069–1089.
[21] Tokay A, Petersen WA, Gatlin P, *et al*. Comparison of raindrop size distribution measurements by collocated disdrometers. *J Atmos Oceanic Technol*. 2013;30(8):1672–1690.
[22] Thurai M, Gatlin P, Bringi VN, *et al*. Toward completing the raindrop size spectrum: case studies involving 2D-video disdrometer, droplet spectrometer, and polarimetric radar measurements. *J Appl Meteor Climatol*. 2017;56(4):877–896.
[23] Thurai M and Bringi VN. Application of the generalized gamma model to represent the full rain drop size distribution spectra. *J Appl Meteor Climatol*. 2018;57(5):1197–1210.

[24] Raupach TH, Thurai M, Bringi VN, *et al*. Reconstructing the drizzle mode of the raindrop size distribution using double-moment normalization. *J Appl Meteor Climatol*. 2019;58(1):145–164.
[25] Willis PT. Functional fits to some observed drop size distributions and parameterization of rain. *J Atmos Sci*. 1984;41(9):1648–1661.
[26] Vivekanandan J, Zhang G, and Brandes E. Polarimetric radar estimators based on a constrained gamma drop size distribution model. *J Appl Meteor*. 2004;43(2):217–230.
[27] Uijlenhoet R. Parameterization of rainfall microstructure for radar meteorology and hydrology; 1999. WU thesis 2734 Proefschrift Wageningen.
[28] Hudson NW. Raindrop size distribution in high intensity storms. *Rhod J Agric Res*. 1963;1:6–11.
[29] Blanchard DC and Spencer AT. Experiments on the generation of raindrop-size distributions by drop breakup. *J Atmos Sci*. 1970;27:101–108.
[30] Brawn D and Upton G. Estimation of an atmospheric gamma drop size distribution using disdrometer data. *Atmos Res*. 2008;87(1):66–79.
[31] Jaffrain J and Berne A. Experimental quantification of the sampling uncertainty associated with measurements from Parsivel disdrometers. *J Hydrometeor*. 2011 June;12(3):329–351.
[32] Park SG, Kim HL, Ham YW, *et al*. Comparative evaluation of the OTT PARSIVEL2 using a collocated two-dimensional video disdrometer. *J Atmos Oceanic Technol*. 2017;34(9):2059–2082.
[33] Gultepe I and Isaac GA. Liquid water content and temperature relationship from aircraft observations and its applicability to GCMs. *J Clim*. 1997;10(3):446–452.
[34] Zwiebel J, Van Baelen J, Anquetin S, *et al*. Topography and rainfall regime impacts on rainfall structure. The case of the HyMeX IOP7a event. *Q J Roy Meteor Soc*. 2015;142(1):310–319.
[35] Dolan B, Fuchs B, Rutledge SA, *et al*. Primary modes of global drop size distributions. *J Atmos Sci*. 2018;75(5):1453–1476.
[36] Heymsfield AJ. Cloud physics. In: Meyers RA, editor, *Encyclopedia of Physical Science and Technology*. 3rd ed. New York, NY: Academic Press; 2003. p. 15–31.
[37] Paul T and Paul TW. Model vertical profile of extreme rainfall rate, liquid water content, and drop size distribution; 1985. Environmental Research Paper No. 926.
[38] Black RA and Hallett J. Rain rate and water content in hurricanes compared with summer rain in Miami, Florida. *J Appl Meteor Climatol*. 2012;51(12):2218–2235.
[39] Atlas S and Ulbrich CW. Path- and area-integrated rainfall measurement by microwave attenuation in the 1–3 cm band. *J Appl Meteor Climatol*. 1977;16(12):1322–1331.
[40] Delrieu G, Hucke L, and Creutin JD. Attenuation in rain for X- and C-band weather radar systems: sensitivity with respect to the drop size distribution. *J Appl Meteor*. 1999;38(1):57–68.

[41] Testud J, Le Bouar E, Obligis E, *et al*. The rain profiling algorithm applied to polarimetric weather radar. *J Atmos Oceanic Technol*. 2000;17(3):332–356.
[42] Park SG, Bringi VN, Chandrasekar V, *et al*. Correction of radar reflectivity and differential reflectivity for rain attenuation at X band. Part I: theoretical and empirical basis. *J Atmos Oceanic Technol*. 2005;22(11):1621–1632.
[43] ITU-R P 838-3. Specific attenuation model for rain for use in prediction methods; 2005. International Telecommunication Union Radiocommunication Recommendations.
[44] van de Hulst HC. Light scattering by small particles. *Q J Roy Meteor Soc*. 1958;84(360):198–199.
[45] Zhang G. Wave scattering by a single particle. In: *Weather Radar P*. 1st ed. Boca Raton, FL: CRC Press; 2016.
[46] Uijlenhoet R, Cohard JM, and Gosset M. Path-average rainfall estimation from optical extinction measurements using a large-aperture scintillometer. *J Hydrometeor*. 2011;12(5):955–972.
[47] Battan LJ. Radar observation of the atmosphere. *Q J Roy Meteor Soc*. 1973;99(422):793–793.
[48] Bringi VN and Chandrasekar V. *Polarimetric Doppler Weather Radar*. Cambridge: Cambridge University Press; 2001.
[49] Beard KV. Terminal velocity and shape of cloud and precipitation drops aloft. *J Atmos Sci*. 1976;33(5):851–864.
[50] Beard KV. Simple altitude adjustments to raindrop velocities for Doppler radar analysis. *J Atmos Oceanic Technol*. 1985;2(4):468–471.
[51] Atlas D, Srivastava R, and Sekhon RS. Doppler radar characteristics of precipitation at vertical incidence. *Rev Geophys*. 1973;11(1):1–35.
[52] Beard KV. Terminal velocity adjustment for cloud and precipitation drops aloft. *J Atmos Sci*. 1977;34(8):1293–1298.
[53] Gunn R and Kinzer GD. The terminal velocity of fall for water droplets in stagnant air. *J Meteor*. 1949;6(4):243–248.
[54] Montero-Martínez G, Kostinski AB, Shaw RA, *et al*. Do all raindrops fall at terminal speed? *Geophys Res Lett*. 2009;36(L11818).
[55] Larsen ML, Kostinski AB, Jameson AR. Further evidence for super-terminal raindrops. *Geophys Res Lett*. 2014;41(19):6914–6918.
[56] Montero-Martínez G, García-García F. On the behaviour of raindrop fall speed due to wind. *Q J Roy Meteor Soc*. 2016;142(698):2013–2020.
[57] Smith JA. Marked point process models of raindrop-size distributions. *J Appl Meteor Climatol*. 1993;32(2):284–296.
[58] Ignaccolo M and De Michele C. A point based Eulerian definition of rain event based on statistical properties of inter drop time intervals: an application to Chilbolton data. *Adv Water Resour*. 2010;33(8):933–941.
[59] Muramoto K, Shiina T, Endoh T, *et al*. Measurement of snowflake size and falling velocity by image processing. In: *Proceedings of the NIPR Symposium on Polar Meteorology and Glaciology*, vol. 2; 1989. p. 48–54.
[60] Sheppard BE. Measurement of raindrop size distributions using a small Doppler radar. *J Atmos Oceanic Technol*. 1990;7(2):255–268.

[61] Notaroš BM, Bringi VN, Kleinkort C, *et al*. Accurate characterization of winter precipitation using multi-angle snowflake camera, visual hull, advanced scattering methods and polarimetric radar. *Atmosphere*. 2016;7(6).
[62] Minda H, Tsuda N, and Fujiyoshi Y. Three-dimensional shape and fall velocity measurements of snowflakes using a multiangle snowflake imager. *J Atmos Oceanic Technol*. 2017;34(8):1763–1781.
[63] Katsuyama Y and Inatsu M. Advantage of volume scanning video disdrometer in solid-precipitation observation. *SOLA*. 2021;17:35–40.
[64] Uijlenhoet R. Raindrop size distributions and radar reflectivity-rain rate relationships for radar hydrology. *Hydrol Earth Syst Sci*. 2001;5(4):615–628.
[65] Krajewski W and Smith J. Radar hydrology: rainfall estimation. *Adv Water Resour*. 2002;25(8):1387–1394.
[66] Krajewski WF, Villarini G, and Smith JA. RADAR-rainfall uncertainties: where are we after thirty years of effort? *Bull Amer Meteor Soc*. 2010;91(1):87–94.
[67] Cristiano E, ten Veldhuis MC, and van de Giesen N. Spatial and temporal variability of rainfall and their effects on hydrological response in urban areas – a review. *Hydrol Earth Syst Sci*. 2017;21(7):3859–3878.
[68] Westbrook CD, Hogan RJ, O'Connor EJ, *et al*. Estimating drizzle drop size and precipitation rate using two-colour lidar measurements. *Atmos Meas Tech*. 2010;3(3):671–681.
[69] WMO. *Guide to Meteorological Instruments and Methods of Observation*. 7th ed. WMO-No.8. Geneva: World Meteorological Organization; 2008.
[70] Segal B. An analytical examination of mathematical models for the rainfall rate distribution function. *Ann Télécommun*. 1980;35(11):434–438.
[71] Bell TL and Suhasini R. Principal modes of variation of rain-rate probability distributions. *J Appl Meteor Climatol*. 1994;33(9):1067–1078.
[72] Benoit L, Allard D, and Mariethoz G. Stochastic rainfall modelling at sub-kilometer scale. *Water Resour Res*. 2018;54(6):4108–4130.
[73] Sekhon RS and Srivastava RC. Doppler radar observations of drop-size distributions in a thunderstorm. *J Atmos Sci*. 1971;28(6):983–994.
[74] Mualem Y and Assouline S. Mathematical-model for rain drop distribution and rainfall kinetic energy. *Trans ASAE*. 1986;29(2):494–500.
[75] Rosewell CJ. Rainfall kinetic energy in eastern Australia. *J Clim Appl Meteor*. 1986;25:1695–1701.
[76] Steiner M and Smith JA. Reflectivity, rain rate, and kinetic energy flux relationships based on raindrop spectra. *J Appl Meteor*. 2000;39(11): 1923.
[77] Kinnell PIA. Raindrop-impact-induced erosion processes and prediction: a review. *Hydrol Process*. 2005;19:2815–2844.
[78] Yu N, Boudevillain B, Delrieu G, *et al*. Estimation of rain kinetic energy from radar reflectivity and/or rain rate based on a scaling formulation of the raindrop size distribution. *Water Resour Res*. 2012;48(4).
[79] Amirzadeh B, Louhghalam A, Raessi M, *et al*. A computational framework for the analysis of rain-induced erosion in wind turbine blades. Part I: stochastic

rain texture model and drop impact simulations. *J Wind Eng Ind Aerod*. 2017;163:33–43.

[80] Bartolomé L and Teuwen J. Methodology for the energetic characterisation of rain erosion on wind turbine blades using meteorological data: a case study for The Netherlands. *Wind Energy*. 2021;24(7):686–698.

[81] Matsumura M, Nomoto M, Itaya T, *et al*. Mechanosensory trichome cells evoke a mechanical stimuli-induced immune response in *Arabidopsis thaliana*. *Nat Commun*. 2022;13(1):1–15.

[82] Gorgucci E, Chandrasekar V, Bringi VN, *et al*. Estimation of raindrop size distribution parameters from polarimetric radar measurements. *J Atmos Sci*. 2002;59(15):2373–2384.

[83] Weber SF. *The Dm Analysis of Precipitation Particle Size Distributions*. Institute of Atmospheric Sciences, South Dakota School of Mines and Technology, Rapid City, SD; 1976. Report 76-14.

[84] Tokay A, D'Adderio LP, Wolff DB, *et al*. Development and evaluation of the raindrop size distribution parameters for the NASA Global Precipitation Measurement mission ground validation program. *J Atmos Oceanic Technol*. 2020;37(1):115–128.

[85] Ryzhkov AV and Zrnic DS. *Radar Polarimetry for Weather Observations*. 1st ed. Cham: Springer; 2019.

[86] Srivastava RC. Size distributions of raindrops generated by their breakup and coalescence. *J Atmos Sci*. 1971;28(3):410–415.

[87] Brazier-Smith PR, Jennings SG, and Latham J. Raindrop interactions and rainfall rates within clouds. *Q J Roy Meteor Soc*. 1973;99(420): 260–272.

[88] List R, Donaldson NR, and Stewart RE. Temporal evolution of drop spectra to collisional equilibrium in steady and pulsating rain. *J Atmos Sci*. 1987;44(2):362–372.

[89] Zawadzki I and De Agostinho Antonio M. Equilibrium raindrop size distributions in tropical rain. *J Atmos Sci*. 1988;45(22):3452–3459.

[90] Sauvageot H and Koffi M. Multimodal raindrop size distributions. *J Atmos Sci*. 2000;57(15):2480–2492.

[91] Gatidis G, Schleiss M, Unal C, *et al*. A critical evaluation of the adequacy of the gamma model for representing raindrop size distributions. *J Atmos Oceanic Technol*. 2020;37(10):1765–1779.

[92] Marshall JS and Palmer WM. The distribution of raindrops with size. *J Meteor*. 1948;5:165–166.

[93] Feingold G and Levin Z. The lognormal fit to raindrop spectra from frontal convective clouds in Israel. *J Appl Meteor Climatol*. 1986;25(10):1346–1363.

[94] Stacy EW. A generalization of the gamma distribution. *Ann Math Stat*. 1962;33(3):1187–1192.

[95] Auf der Maur AN. Statistical tools for drop size distributions: moments and generalized gamma. *J Atmos Sci*. 2001;58(4):407–418.

[96] Best AC. The size distribution of raindrops. *Q J Roy Meteor Soc*. 1950;76(327):16–36.

[97] Bardsley WE. Note on y-truncation: a simple approach to generating bounded distributions for environmental applications. *Adv Water Resour*. 2007;30(1):113–117.

[98] Cugerone K and De Michele C. Johnson SB as general functional form for raindrop size distribution. *Water Resour Res*. 2015;51(8):6276–6289.

[99] Yangang L. Statistical theory of the Marshall-Palmer distribution of raindrops. *Atmos Environ A—Gen*. 1993;27(1):15–19.

[100] Tokay A and Short DA. Evidence from tropical raindrop spectra of the origin of rain from stratiform versus convective clouds. *J Appl Meteor*. 1996;35(3):355–371.

[101] Smith PL. Raindrop size distributions: exponential or gamma – does the difference matter? *J Appl Meteor*. 2003;42(7):1031–1034.

[102] Zhang G, Vivekanandan J, and Brandes E. A method for estimating rain rate and drop size distribution from polarimetric radar measurements. *IEEE Trans Geosci Remote Sens*. 2001;39(4):830–841.

[103] Zhang G, Vivekanandan J, Brandes EA, *et al*. The shape-slope relation in observed gamma raindrop size distributions: statistical error or useful information? *J Atmos Oceanic Technol*. 2003;20(8):1106–1119.

[104] Lee G, Zawadzki I, Szyrmer W, *et al*. A general approach to double-moment normalization of drop size distributions. *J Appl Meteor*. 2004;43(2):264–281.

[105] Jiang H, Sano M, and Sekine M. Weibull raindrop-size distribution and its application to rain attenuation. *IEE P-Microw Anten P*. 1997;144:197–200(3).

[106] Sekine M, Ishii S, Hwang SI, *et al*. Weibull raindrop-size distribution and its application to rain attenuation from 30 GHz to 1000 GHz. *Int J Infrared Milli*. 2007;28(5):383–392.

[107] Cugerone K and De Michele C. Investigating rain drop size distributions in the (L-)Skewness-(L-)Kurtosis plane. *Q J Roy Meteor Soc*. 2017;143(704): 1303–1312.

[108] Testud J, Oury S, Black RA, *et al*. The concept of "normalized" distribution to describe raindrop spectra: a tool for cloud physics and cloud remote sensing. *J Appl Meteor*. 2001;40(6):1118–1140.

[109] Illingworth AJ and Blackman TM. The need to represent raindrop size spectra as normalized gamma distributions for the interpretation of polarization radar observations. *J Appl Meteor*. 2002;41(3):286–297.

[110] Laws JO and Parsons DA. The relation of raindrop-size to intensity. *Eos, Trans Am Geophys Union*. 1943;24(2):452–460.

[111] Sempere-Torres D, Porrà JM, and Creutin JD. A general formulation for raindrop size distribution. *J Appl Meteor*. 1994;33(12):1494–1502.

[112] Sempere-Torres D, Sanchez-Diezma R, Zawadzki I, *et al*. Identification of stratiform and convective areas using radar data with application to the improvement of DSD analysis and *ZR* relations. *Phys Chem Earth Part B*. 2000;25(10):985–990.

[113] Yu N, Delrieu G, Boudevillain B, *et al*. Unified formulation of single- and multimoment normalizations of the raindrop size distribution based on the gamma probability density function. *J Appl Meteor Climatol*. 2014;53(1):166–179.

[114] Morrison H, Kumjian MR, Martinkus CP, *et al*. A general n-moment normalization method for deriving raindrop size distribution scaling relationships. *J Appl Meteor Climatol*. 2019;58(2):247–267.
[115] Ignaccolo M and Michele CD. Phase space parameterization of rain: the inadequacy of gamma distribution. *J Appl Meteor Climatol*. 2014;53(2): 548–562.
[116] Raupach TH and Berne A. Invariance of the double-moment normalized raindrop size distribution through 3D spatial displacement in stratiform rain. *J Appl Meteor Climatol*. 2017;56(6):1663–1680.
[117] Porrà JM, Sempere-Torres D, and Creutin JD. Modeling of drop size distribution and its applications to rainfall measurements from radar. In: *Stochastic Methods in Hydrology*, vol. 7. Singapore: World Scientific; 1998. p. 73–84.
[118] Sempere-Torres D, Porrà JM, and Creutin JD. Experimental evidence of a general description for raindrop size distribution properties. *J Geophys Res: Atmos*. 1998;103(D2):1785–1797.
[119] Berne A, Jaffrain J, and Schleiss M. Scaling analysis of the variability of the rain drop size distribution at small scale. *Adv Water Resour*. 2012;45:2–12.
[120] Bringi V, Huang GJ, Chandrasekar V, *et al*. A methodology for estimating the parameters of a gamma raindrop size distribution model from polarimetric radar data: application to a squall-line event from the TRMM/Brazil campaign. *J Atmos Oceanic Technol*. 2002;19(5):633–645.
[121] Chandrasekar V, Li W, and Zafar B. Estimation of raindrop size distribution from spaceborne radar observations. *IEEE Trans Geosci Remote Sens*. 2005;43(5):1078–1086.
[122] Seto S, Iguchi T, and Oki T. The basic performance of a precipitation retrieval algorithm for the Global Precipitation Measurement mission's single/dual-frequency radar measurements. *IEEE Trans Geosci Remote Sens*. 2013;51(12):5239–5251.
[123] Grecu M, Olson WS, Munchak SJ, *et al*. The GPM combined algorithm. *J Atmos Oceanic Technol*. 2016;33(10):2225–2245.
[124] Seliga T and Bringi V. Potential use of radar differential reflectivity measurements at orthogonal polarizations for measuring precipitation. *J Appl Meteor*. 1976;15(1):69–76.
[125] Ryzhkov AV. Interpretation of polarimetric radar covariance matrix for meteorological scatterers: theoretical analysis. *J Atmos Oceanic Technol*. 2001;18(3):315–328.
[126] Zrnic DS and Ryzhkov AV. Advantages of rain measurements using specific differential phase. *J Atmos Oceanic Technol*. 1996;13(2):454–464.
[127] Marshall JS, Hitschfeld W, and Gunn KLS. Advances in radar weather. *Adv Geophys*. 1955;2:1–56.
[128] Chen H and Chandrasekar V. The quantitative precipitation estimation system for Dallas-Fort Worth (DFW) urban remote sensing network. *J Hydrol*. 2015;531(2):259–271.
[129] Seifert A. On the shape–slope relation of drop size distributions in convective rain. *J Appl Meteor*. 2005;44(7):1146–1151.

[130] Moisseev DN and Chandrasekar V. Examination of the μ-λ relation suggested for drop size distribution parameters. *J Atmos Oceanic Technol*. 2007;24(5):847–855.

[131] Raupach TH and Berne A. Retrieval of the raindrop size distribution from polarimetric radar data using double-moment normalisation. *Atmos Meas Tech*. 2017;10(7):2573–2594.

[132] Bringi V, Mishra KV, Thurai M, *et al*. Retrieval of lower-order moments of the drop size distribution using CSU-CHILL X-band polarimetric radar: a case study. *Atmos Meas Tech*. 2020;13(9):4727–4750.

[133] Schneebeli M, Grazioli J, and Berne A. Improved estimation of the specific differential phase shift using a compilation of Kalman filter ensembles. *IEEE Trans Geosci Remote Sens*. 2014;52(8):5137–5149.

[134] Huang H, Zhang G, Zhao K, *et al*. Uncertainty in retrieving raindrop size distribution from polarimetric radar measurements. *J Atmos Oceanic Technol*. 2019;36(4):585–605.

[135] Vulpiani G, Marzano FS, Chandrasekar V, *et al*. Polarimetric weather radar retrieval of raindrop size distribution by means of a regularized artificial neural network. *IEEE Trans Geosci Remote Sens*. 2006;44(11): 3262–3275.

[136] Kalogiros J, Anagnostou MN, Anagnostou EN, *et al*. Optimum estimation of rain microphysical parameters from X-band dual-polarization radar observables. *IEEE Trans Geosci Remote Sens*. 2013;51(5): 3063–3076.

[137] Kumjian MR, Prat OP, Collis S, *et al*. A moment-based polarimetric radar forward operator for rain microphysics. *J Appl Meteor Climatol*. 2019;58(1): 113–130.

[138] Conrick R, Zagrodnik JP, and Mass CF. Dual-polarization radar retrievals of coastal Pacific Northwest raindrop size distribution parameters using random forest regression. *J Atmos Oceanic Technol*. 2020;37(2):229–242.

[139] Yang Q, Dai Q, Zhang S, *et al*. Raindrop size distribution retrieval model for x-band dual-polarization radar in China incorporating various climatic and geographical elements. *IEEE Trans Geosci Remote Sens*. 2022;60:1–17.

[140] Williams CR. Simultaneous ambient air motion and raindrop size distributions retrieved from uhf vertical incident profiler observations. *Radio Sci*. 2002;37(2):1–13.

[141] Peters G, Fischer B, Münster H, *et al*. Profiles of raindrop size distributions as retrieved by micro rain radars. *J Appl Meteor*. 2005;44(12):1930–1949.

[142] Le M and Chandrasekar V. An algorithm for drop-size distribution retrieval from GPM dual-frequency precipitation radar. *IEEE Trans Geosci Remote Sens*. 2014;52(11):7170–7185.

[143] Mróz K, Battaglia A, Kneifel S, *et al*. Triple-frequency Doppler retrieval of characteristic raindrop size. *Earth Space Sci*. 2020;7(3):e2019EA000789.

[144] Unal C. High-resolution raindrop size distribution retrieval based on the Doppler spectrum in the case of slant profiling radar. *J Atmos Oceanic Technol*. 2015;32(6):1191–1208.

[145] Weisman ML, Skamarock WC, and Klemp JB. The resolution dependence of explicitly modeled convective systems. *Mon Weather Rev*. 1997;125(4): 527–548.
[146] Arakawa A. The cumulus parameterization problem: past, present, and future. *J Clim*. 2004;17(13):2493–2525.
[147] Morrison H, van Lier-Walqui M, Fridlind AM, *et al*. Confronting the challenge of modeling cloud and precipitation microphysics. *J Adv Model Earth Syst*. 2020;12(8):e2019MS001689.
[148] Khain AP, Beheng KD, Heymsfield A, *et al*. Representation of microphysical processes in cloud-resolving models: spectral (bin) microphysics versus bulk parameterization. *Rev Geophys*. 2015;53(2):247–322.
[149] Randall DA, Bitz CM, Danabasoglu G, *et al*. 100 years of Earth system model development. *Meteor Mon*. 2018;59:12.1–12.66.
[150] Kessler E. On the distribution and continuity of water substance in atmospheric circulations. In: *Meteorological Monographs*. Boston, MA: American Meteorological Society; 1969. p. 1–84.
[151] Lin YL, Farley RD, and Orville HD. Bulk parameterization of the snow field in a cloud model. *J Appl Meteor Climatol*. 1983;22(6):1065–1092.
[152] Thompson G, Field PR, Rasmussen RM, *et al*. Explicit forecasts of winter precipitation using an improved bulk microphysics scheme. Part II: implementation of a new snow parameterization. *Mon Weather Rev*. 2008;136(12):5095–5115.
[153] Igel AL, Igel MR, and van den Heever SC. Make it a double? Sobering results from simulations using single-moment microphysics schemes. *J Atmos Sci*. 2015;72(2):910–925.
[154] Schoenberg Ferrier B. A double-moment multiple-phase four-class bulk ice scheme. Part I: description. *J Atmos Sci*. 1994;51(2):249–280.
[155] Cohard JM and Pinty JP. A comprehensive two-moment warm microphysical bulk scheme. I: description and tests. *Q J Roy Meteor Soc*. 2000;126(566):1815–1842.
[156] Seifert A and Beheng KD. A double-moment parameterization for simulating autoconversion, accretion and selfcollection. *Atmos Res*. 2001;59-60: 265–281.
[157] Morrison H, Thompson G, and Tatarskii V. Impact of cloud microphysics on the development of trailing stratiform precipitation in a simulated squall line: comparison of one- and two-moment schemes. *Mon Weather Rev*. 2009;137(3):991–1007.
[158] Milbrandt JA and Yau MK. A multimoment bulk microphysics parameterization. Part II: a proposed three-moment closure and scheme description. *J Atmos Sci*. 2005;62(9):3065–3081.
[159] Shipway BJ and Hill AA. Diagnosis of systematic differences between multiple parametrizations of warm rain microphysics using a kinematic framework. *Q J Roy Meteor Soc*. 2012;138(669):2196–2211.
[160] Loftus AM, Cotton WR, and Carrió GG. A triple-moment hail bulk microphysics scheme. Part I: description and initial evaluation. *Atmos Res*. 2014;149:35–57.

[161] Naumann AK and Seifert A. Evolution of the shape of the raindrop size distribution in simulated shallow cumulus. *J Atmos Sci*. 2016;73(6): 2279–2297.

[162] Paukert M, Fan J, Rasch PJ, *et al*. Three-moment representation of rain in a bulk microphysics model. *J Adv Model Earth Syst*. 2019;11(1): 257–277.

[163] Kogan YL and Belochitski A. Parameterization of cloud microphysics based on full integral moments. *J Atmos Sci*. 2012;69(7):2229–2242.

[164] Reisin T, Levin Z, and Tzivion S. Rain production in convective clouds as simulated in an axisymmetric model with detailed microphysics. Part I: description of the model. *J Atmos Sci*. 1996;53(3):497–519.

[165] Khain A, Pokrovsky A, Pinsky M, *et al*. Simulation of effects of atmospheric aerosols on deep turbulent convective clouds using a spectral microphysics mixed-phase cumulus cloud model. Part I: model description and possible applications. *J Atmos Sci*. 2004;61(24):2963–2982.

[166] Beheng KD. A parameterization of warm cloud microphysical conversion processes. *Atmos Res*. 1994;33(1):193–206. *11th International Conference on Clouds and Precipitation, Part II*.

[167] Morrison H and Grabowski WW. Comparison of bulk and bin warm-rain microphysics models using a kinematic framework. *J Atmos Sci*. 2007;64(8):2839–2861.

[168] Shima S, Kusano K, Kawano A, *et al*. The super-droplet method for the numerical simulation of clouds and precipitation: a particle-based and probabilistic microphysics model coupled with a non-hydrostatic model. *Q J Roy Meteor Soc*. 2009;135(642):1307–1320.

[169] Riechelmann T, Noh Y, and Raasch S. A new method for large-eddy simulations of clouds with Lagrangian droplets including the effects of turbulent collision. *New J Phys*. 2012;14(6):065008.

[170] Grabowski WW. Comparison of Eulerian bin and Lagrangian particle-based schemes in simulations of Pi chamber dynamics and microphysics. *J Atmos Sci*. 2020;77(3):1151–1165.

[171] Morrison H, Witte M, Bryan GH, *et al*. Broadening of modeled cloud droplet spectra using bin microphysics in an Eulerian spatial domain. *J Atmos Sci*. 2018;75(11):4005–4030.

[172] Vivekanandan J, Zrnic DS, Ellis SM, *et al*. Cloud microphysics retrieval using S-band dual-polarization radar measurements. *Bull Amer Meteor Soc*. 1999;80(3):381–388.

[173] Zhang G, Sun J, and Brandes EA. Improving parameterization of rain microphysics with disdrometer and radar observations. *J Atmos Sci*. 2006;63(4):1273–1290.

[174] Firda JM, Sekelsky SM, and McIntosh RE. Application of dual-frequency millimeter-wave Doppler spectra for the retrieval of drop size distributions and vertical air motion in rain. *J Atmos Oceanic Technol*. 1999;16(2):216–236.

[175] Tridon F and Battaglia A. Dual-frequency radar Doppler spectral retrieval of rain drop size distributions and entangled dynamics variables. *J Geophys Res: Atmos*. 2015;120(11):5585–5601.

[176] Tridon F, Battaglia A, Luke E, *et al*. Rain retrieval from dual-frequency radar Doppler spectra: validation and potential for a midlatitude precipitating case-study. *Q J Roy Meteor Soc*. 2017;143(704):1364–1380.
[177] Kumjian MR and Ryzhkov AV. The impact of evaporation on polarimetric characteristics of rain: theoretical model and practical implications. *J Appl Meteor Climatol*. 2010;49(6):1247–1267.
[178] Kumjian MR and Ryzhkov AV. The impact of size sorting on the polarimetric radar variables. *J Atmos Sci*. 2012;69(6):2042–2060.
[179] Kumjian MR and Prat OP. The impact of raindrop collisional processes on the polarimetric radar variables. *J Atmos Sci*. 2014;71(8):3052–3067.
[180] Lee G and Zawadzki I. Variability of drop size distributions: noise and noise filtering in disdrometric data. *J Appl Meteor*. 2005;44(5):634–652.
[181] Raupach TH and Berne A. Correction of raindrop size distributions measured by Parsivel disdrometers, using a two-dimensional video disdrometer as a reference. *Atmos Meas Tech*. 2015;8(1):343–365.
[182] Tapiador FJ, Sánchez JL, and García-Ortega E. Empirical values and assumptions in the microphysics of numerical models. *Atmos Res*. 2019;215: 214–238.
[183] Szyrmer W, Laroche S, and Zawadzki I. A microphysical bulk formulation based on scaling normalization of the particle size distribution. Part I: description. *J Atmos Sci*. 2005;62(12):4206–4221.